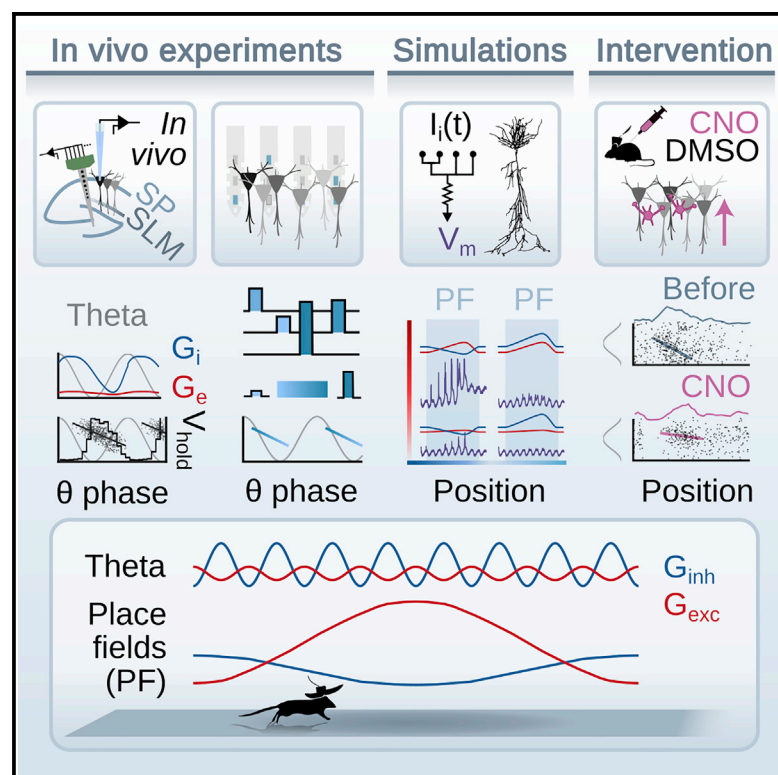


Inhibitory conductance controls place field dynamics in the hippocampus

Graphical abstract



Authors

Manuel Valero, Andrea Navas-Olive,
Liset M. de la Prida, György Buzsáki

Correspondence

Imprida@cajal.csic.es (L.M.d.l.P.),
gyorgy.buzsaki@nyumc.org (G.B.)

In brief

Valero et al. examine the influence of inhibition on place fields. They show that hippocampal neurons are dominated by inhibitory conductances during theta oscillations. A transient increase of excitation and drop of inhibition mediates place field emergence in simulations. Consistently, chemogenetic activation of interneurons deteriorates place cell properties *in vivo*.

Highlights

- Inhibition dominates over excitation during theta oscillations in the CA1 region
- Concerted excitation/disinhibition favors place field properties in simulations
- DREADDs activation of interneurons impairs place field features in CA1
- A transient decrease of inhibition is critical for place field expression



Article

Inhibitory conductance controls place field dynamics in the hippocampus

Manuel Valero,^{1,5} Andrea Navas-Olive,^{2,5} Liset M. de la Prida,^{2,*} and György Buzsáki^{1,3,4,6,*}
¹Neuroscience Institute, Langone Medical Center, New York University, New York, NY 10016, USA

²Instituto Cajal, Consejo Superior de Investigaciones Científicas, Avenue Doctor Arce 37, Madrid 28002, Spain

³Center for Neural Science, New York University, New York, NY 10003, USA

⁴Department of Neurology, Langone Medical Center, New York, NY 10016, USA

⁵These authors contributed equally

⁶Lead contact

*Correspondence: lmprida@cajal.csic.es (L.M.d.l.P.), gyorgy.buzsaki@nyumc.org (G.B.)

<https://doi.org/10.1016/j.celrep.2022.111232>

SUMMARY

Hippocampal place cells receive a disparate collection of excitatory and inhibitory currents that endow them with spatially selective discharges and rhythmic activity. Using a combination of *in vivo* intracellular and extracellular recordings with opto/chemogenetic manipulations and computational modeling, we investigate the influence of inhibitory and excitatory inputs on CA1 pyramidal cell responses. At the cell bodies, inhibition leads and is stronger than excitation across the entire theta cycle. Pyramidal neurons fire on the ascending phase of theta when released from inhibition. Computational models equipped with the observed conductances reproduce these dynamics. In these models, place field properties are favored when the increased excitation is coupled with a reduction of inhibition within the field. As predicted by our simulations, firing rate within place fields and phase locking to theta are impaired by DREADDs activation of interneurons. Our results indicate that decreased inhibitory conductance is critical for place field expression.

INTRODUCTION

Understanding how local circuits change yet maintain their own dynamics in response to intermittently occurring inputs is necessary for revealing the transformation rules of local computation. The hippocampal CA1 region is a unique case because of its weak and sparse excitatory recurrence and because it receives unidirectional afferents from both layer 3 of the entorhinal cortex and the CA3 region (Andersen et al., 2009; Deuchars and Thomson, 1996). Based mainly on anatomical considerations, it has been postulated that the firing patterns of CA1 pyramidal neurons are largely “inherited” or induced by these upstream regions (Ahmed and Mehta, 2009; Grienberger et al., 2017; Hafting et al., 2005; Mizumori et al., 1989; Rolls et al., 2006; Savelli and Knierim, 2010; Skaggs et al., 1996; Solstad et al., 2006; Steffenach et al., 2005).

One of the most studied dynamic patterns in the CA1 region is spatially tuned firing of pyramidal neurons (O’Keefe and Nadel, 1978). When an animal explores its environment, a fraction of pyramidal neurons becomes sequentially active along its movement path. Transient cell assemblies, presumably activated by external “spatial inputs,” fire rhythmically and at a frequency faster than the summed membrane potentials of the majority of pyramidal neurons, as reflected by the local field potential (LFP) theta rhythm (O’Keefe and Recce, 1993). Consequently, the interference between the faster oscillating active cell assembly and background theta rhythm is reflected by “phase

precession” of place cell spikes relative to the ongoing LFP theta oscillation (O’Keefe and Recce, 1993; Skaggs et al., 1996). This theta “phase coding” has been shown to be more spatially precise, especially at shorter time scales, than relating on positional firing rates (Lisman, 2005; O’Keefe and Recce, 1993). An alternative formulation is that the CA1 circuit is endowed with the computational capacity to generate assembly sequences, which are detected secondarily as sequentially active place fields during maze performance (Dragoi and Tonegawa, 2010; Grosmark and Buzsáki, 2016; McKenzie et al., 2021; Valero et al., 2022; Zutshi et al., 2022). In support of this view, recent studies have shown that functional deafferentation of CA1 from upstream inputs has limited impact on the fraction of observable CA1 place fields (Fernández-Ruiz et al., 2021; Kanter et al., 2017; Latuske et al., 2018; Miao et al., 2015; Rueckemann et al., 2016; Zutshi et al., 2022).

The implication of this latter view is that the main features of the CA1 dynamics largely emerge from its local circuit, while upstream inputs play a role in selecting the initial condition for sequences. For single place cells, these features include slow depolarization and increased amplitude of intracellular theta rhythm within the place field and phase precession of the emitted spikes relative to the extracellularly recorded theta cycle (Grienberger et al., 2017; Harvey et al., 2009). Phase precession appears to involve a consortium of circuit and single neuron mechanisms (Figure 1A; Burgess et al., 1994; Fernández-Ruiz et al., 2017; Harvey et al., 2009; Hasselmo et al., 2002; Jensen



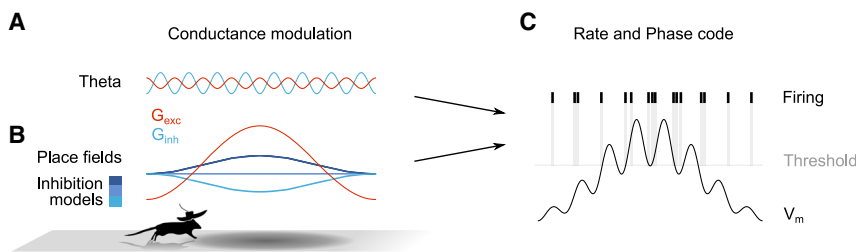


Figure 1. Hypothetical dynamics of excitatory and inhibitory conductances underlying place field features

(A) Co-occurring rhythmic excitatory (red) and inhibitory (blue) conductances in pyramidal neurons during theta oscillations.

(B) Hypothetical mechanisms underlying spatially modulated V_m changes during place field traversal. The assumed slow excitation may be coupled with increasing or decreasing in-field inhibition or spatially uniform inhibition (different shades of blue).

(C) As the animal traverses the cell place field, the interplay between theta-rhythmic conductances and the spatially modulated slow excitation affects both in-field firing rate and theta phase relationship of spiking.

and Lisman, 2000; Kamondi et al., 1998; Magee, 2001; Skaggs et al., 1996). A key common variable in the different models is the relationship between excitation and inhibition within and outside the place field, which has been the subject of intense debate, due mainly to the paucity of observational data (Grienberger et al., 2017; Harvey et al., 2009; Lapray et al., 2012; Royer et al., 2012). Perisomatic inhibitory drive within the place field has been proposed to increase (Bhatia et al., 2019; Milstein et al., 2021), remain unchanged (Grienberger et al., 2017), or decrease (Geiller et al., 2022; Valero et al., 2022) inside the place field (Figure 1B). Yet, how competition between excitatory and inhibitory conductances contributes to the fundamental properties of place cells has remained largely unexplained (Figure 1C).

To investigate the role of inhibition in theta rhythmicity and spatial modulation in the hippocampus, we combined intracellular and extracellular recordings with computational modeling and optogenetic/chemogenetic manipulations. We observed that outside the place field, the inhibitory conductance is several times stronger than the excitatory conductance, and that inhibition precedes excitation in each theta cycle. Our key observation is that decreased inhibitory conductance is an important contributor to spike discharge dynamics, in line with recent works showing a downmodulation of the inhibitory inputs alongside place fields (Geiller et al., 2022; Valero et al., 2022). Constrained by our observations, we analyzed how inhibitory and excitatory conductances interact with upstream spatial inputs in a single neuron model and, in turn, tested the model predictions by pharmacogenetic activation of interneurons. Our findings suggest that the spatial tuning of local inhibition is a fundamental mechanism of both rate and phase coding in the hippocampal CA1 region.

RESULTS

Excitatory and inhibition conductances during theta oscillations

To probe the synaptic mechanism of theta phase locking of spikes, we combined intracellular and multi-site silicon probe recordings (16–64 channels) in the dorsal CA1 region of anesthetized rats and awake head-fixed mice (Figure 2A; 11 cells from 10 rats and seven cells from four mice; Figures S1A–S1C). The intracellular membrane potential (V_m) oscillations were coherent with the LFP. As previously reported (Nuñez et al., 1990; Soltesz and Deschenes, 1993; Ylinen et al., 1995), the peak of the intracellular depolarization measured at the resting potential (0 nA

holding current) lagged ($76^\circ \pm 35^\circ$) behind the trough (negative polarity peak) of theta cycles (π) recorded in the CA1 pyramidal layer. Both the phase and amplitude of the intracellular theta depended on the holding potential of the neuron (Figure 2B). Depolarizing current injection increased the amplitude of the intracellular theta, whereas hyperpolarization decreased it, reaching a minimum at approximately -75 mV. With further hyperpolarization, the theta amplitude increased again, associated with the reversal of theta cycle phase (Figure 2B; Figures S1D–S1G; Soltesz and Deschenes, 1993; Ylinen et al., 1995).

It has been proposed that these V_m -dependent changes arise from an interaction of phase-shifted rhythmic inhibitory synaptic inputs to the soma and excitatory inputs to the dendrites (Leung, 1984; Navas-Olive et al., 2020). To dissect these inhibitory and excitatory components, we first estimated the total synaptic conductance ($G(t)$) during theta cycles from the slope (I/V curve) of the linear regression of the estimated current flow ($I = V_m$ divided by the measured input resistance, $\Delta V_m(t)/R_m$) and the holding potential (V_{hold}) (Valero et al., 2017). From this relationship, we derived the excitatory and inhibitory conductances (G_{exc} and G_{inh}) using their respective reversal potentials (-75 mV and 0 mV for inhibitory and excitatory reversal potentials, respectively; STAR Methods; Borg-Graham et al., 1998; Ylinen et al., 1995). On average, G_{inh} peak, measured in the soma, was larger and preceded the peak of G_{exc} (Figures 2C and S2A–S2C), corresponding to a total inhibition-to-excitation conductance ratio of 6.7 ± 1.4 (Figure S2D). The G_{exc} peak matched the reported firing phase of the CA3 pyramidal cells at the falling phase of theta (Mizuseki et al., 2009; Valero and de la Prida, 2018), while G_{inh} mirrored the preferred firing phase of perisomatic parvalbumin (PV) and cholecystokinin (CCK)-expressing basket cells and axo-axonic cells (Klausberger et al., 2005; Lapray et al., 2012; Valero and de la Prida, 2018; Viney et al., 2013).

Because our estimation of G_{exc} and G_{inh} may fall short to integrate the contribution of poorly current-clamped distal dendrites (Borg-Graham et al., 1998) and to test the sufficiency of these experimentally obtained conductances, we reverse-engineered our results in a single neuron model. We built a single-compartment passive model, which included oscillatory inhibitory and excitatory inputs derived from the estimated conductances (Figure 2D). We then injected current (I_{hold}) to clamp the simulated neuron at different holding voltages as we did in our experiments (Figure 2E). The model replicated the same voltage-dependent changes of both theta amplitude and phase as observed in our

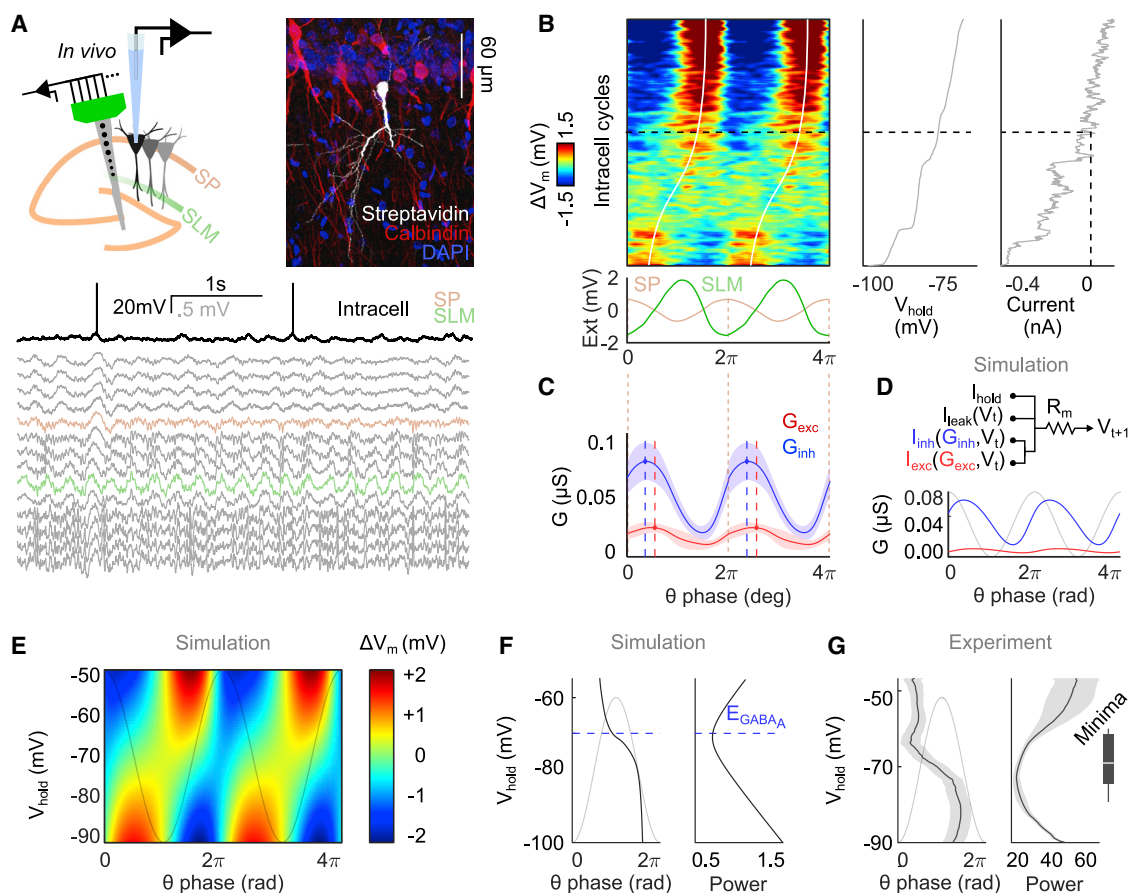


Figure 2. In vivo measurement of theta conductances and data-driven single cell model

(A) Simultaneous intracellular and extracellular recordings in an anesthetized rat. Image of a CA1 pyramidal neuron filled with biocytin. Intracellular (black) and simultaneous silicon probe-recorded LFP (gray) traces. Traces from pyramidal layer (SP, orange) and str. lacunosum-moleculare (SLM green). (B) Theta phase of membrane potential change with respect to V_{hold} (ΔV_m , left) at different holding potentials from the same cell as in (A). Each row is a V_m trace during two theta cycles, sorted by V_{hold} (middle). Right, injected current and corresponding holding potential (V_{hold}). Bottom, average LFP theta from SP and SLM. (C) Average excitatory and inhibitory conductances (G_{exc} and G_{inh} , respectively) estimated from 18 CA1 pyramidal cells recorded from 10 anesthetized rats and four awake, head-fixed mice. The amplitude of G_{inh} is markedly larger, and G_{inh} peaks earlier than G_{exc} . (D) Single-compartment passive model with asymmetric I_{inh} and I_{exc} obtained from the observed conductances in (C). Leak (I_{leak}) and holding currents (I_{hold}) were also added. (E) Simulated ΔV_m as function of the injected current in the model neuron. (F) Left, theta phase reversal of V_m occurs at V_{hold} close to the simulated $GABA_A$ reversal (blue dashed line). Right, theta power of V_m . (G) Similar display as in (F), but from all intracellularly recorded pyramidal cells. Inset shows distribution of V_{hold} corresponding to minimum of intracellular theta power.

intracellular recordings (Figures 2F and 2G). The theta phase reversal and the minimum theta power were consistently present at I_{hold} near the simulated $GABA_A$ reversal (-75 mV; Figures 2F and 2G). These experiments suggest that during theta oscillations synaptic inhibition dominates over excitation in the somata of pyramidal cells and that excitatory inputs lag behind somatic inhibition. This relationship is also supported by the reported phase preferences of the main excitatory and perisomatic inhibitory neuronal populations to the CA1 region (Klausberger et al., 2005; Mizuseki et al., 2009).

Membrane voltage affects firing phase

In our model, we investigated how competition between G_{exc} and G_{inh} controls spike timing in pyramidal neuron. Spike prob-

ability and timing depend on the combinations of somato-dendritic synaptic inputs, V_m trajectory, and the spiking history of the neuron. As previously reported, action potentials of the majority of CA1 pyramidal cells occurred at highest probability close the trough (π or 180°) of the theta cycle recorded in the pyramidal layer (Figures 3A and 3B; Buzsáki et al., 1983; Navas-Olive et al., 2020), although phase preference for the theta cycle peak (0°) has also been reported, depending on the brain state, input integration, and pyramidal cell subtype (Fernández-Ruiz et al., 2017; Mizuseki et al., 2011; Navas-Olive et al., 2020). V_m depolarization peaks correlated with the maximal spiking probability of the cells during theta oscillations (Figures 3A and 3B; Ylinen et al., 1995), where inhibitory conductance reached a minimum (Figures 3A and 3C). The holding potential (V_{hold}) also influenced the spiking

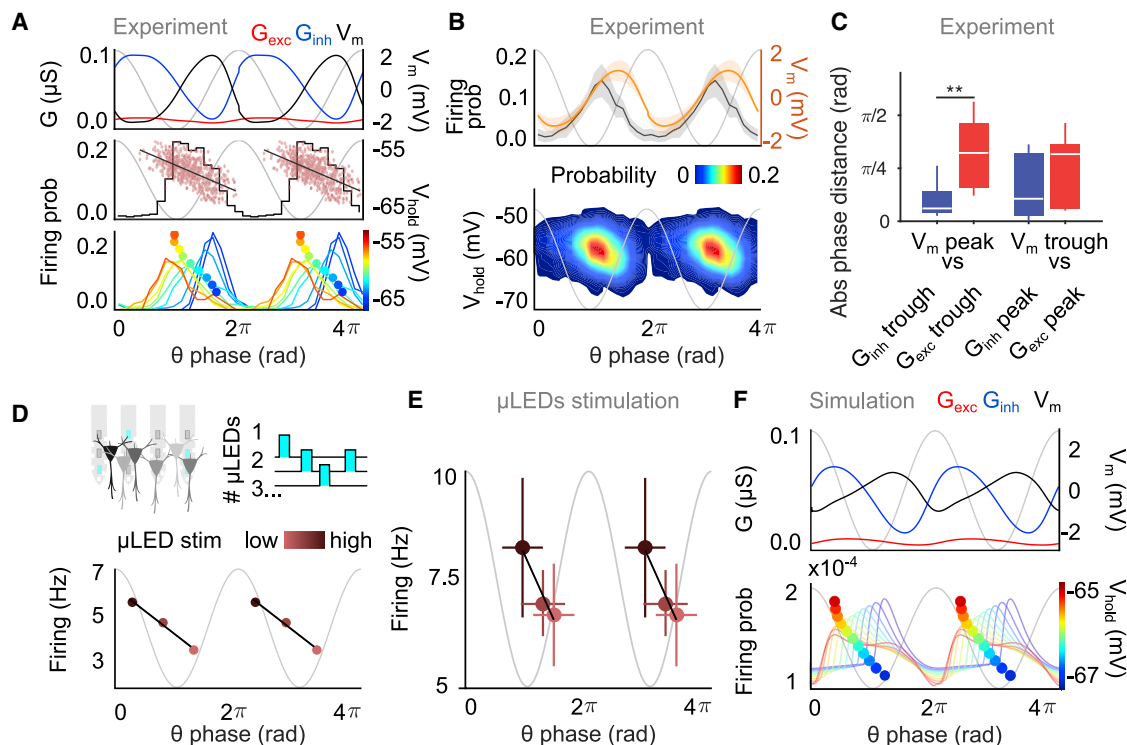


Figure 3. Membrane potential dynamics affect theta phase-related spiking

(A) Top, V_m and the associated G_{exc} and G_{inh} , estimated from an intracellularly recorded CA1 pyramidal cell during theta oscillations (anesthetized rat). Middle, theta phase-locking spike histogram of the same neuron. Each dot represents an action potential. Bottom, phase distribution of spikes groups emitted at different holding potentials (0.5 mV step bins). With increasing depolarization, the spike threshold coincides with earlier theta phases.

(B) Top, average theta phase locking of discharge probability (black) with overlaid V_m change (orange). Bottom, theta phase preference versus holding potential (V_{hold}) for all recorded cells ($n = 11$ cells from 10 anesthetized rats, $n = 7$ cells from four head-fixed mice).

(C) Average phase lag between peak and trough for V_m and the estimated G_{inh} and G_{exc} . V_m peak concurs at more strongly with G_{inh} than with G_{exc} ($Z_{MS} = 9.33$, $p = 0.002$; multiple-sample (MS) test for equal median directions; V_m trough lag: $Z_{MS} = 2.34$, $p = 0.12$; MS test).

(D) Theta phase locking of optogenetic fast-pulse induced spikes in a representative CA1 pyramidal cell at three different light intensities (dots; two consecutive cycles are plotted).

(E) Preferred theta phases of the induced spikes in 63 pyramidal neurons at increasing light intensities (linear-circular correlation coefficient $\rho = -0.45 \pm 0.62$).

(F) Same display as in (A), but from the single-compartment passive model. *** $p < 0.001$.

phase preference. At more depolarized voltages, action potentials occurred at earlier theta phases, resulting in voltage-dependent phase precession (Figures 3A and 3B), in line with prior both *in vitro* (Magee, 2001) and *in vivo* (Kamondi et al., 1998) studies. This phase advance occurred because the spike threshold was reached at an earlier theta phase at more depolarized membrane potentials (see V_m line in Figure 3A).

To reproduce the model-predicted correlation experimentally in a larger population of pyramidal neurons, we exploited a high-throughput optogenetic probing method to track for theta phase subthreshold dynamics in freely behaving CamKII α -Cre:Ai32 mice (Valero et al., 2022). Mice ($n = 4$) were implanted with four-shank μ LED probes with three μ LEDs/shank (Valero et al., 2022; Wu et al., 2015) to induce 20-ms light pulses at random intervals (Valero et al., 2022). For these experiments, we included only neurons that showed significant spike responses to each of the three different light intensity levels (63 pyramidal cells). Optogenetic depolarization, similar to intracellular current injection, increased the firing rate of the neuron and advanced the phase of preferred spiking (Figures 3D and 3E).

To evaluate the preferred phase of spiking at different V_{hold} in our single-compartment neuron model, firing probability was derived from the simulated membrane potential by a linear activation function (Figure S3 and STAR Methods). As expected, depolarization of the model neuron advanced the preferred phase of firing (Figure 3F), similar to the *in vivo* observations (compare with Figure 3A; Kamondi et al., 1998). In summary, our conductance-based model reliably mimicked the subthreshold and firing dynamics (Figures 2 and 3, respectively) observed in our intracellular and extracellular recordings from CA1 pyramidal cells during theta oscillations.

Place field-tuned excitatory and inhibitory conductances

Next, we sought to understand how variations in the excitatory (Davoudi and Foster, 2019; Zutshi et al., 2022) and inhibitory inputs (Geiller et al., 2022; Royer et al., 2012; Valero et al., 2022) of a pyramidal neuron could contribute to place-field-related activity. Spatial modulation (McClain et al., 2019; Tsodyks et al., 1996) was added to our model as a skewed Gaussian-like (Harvey

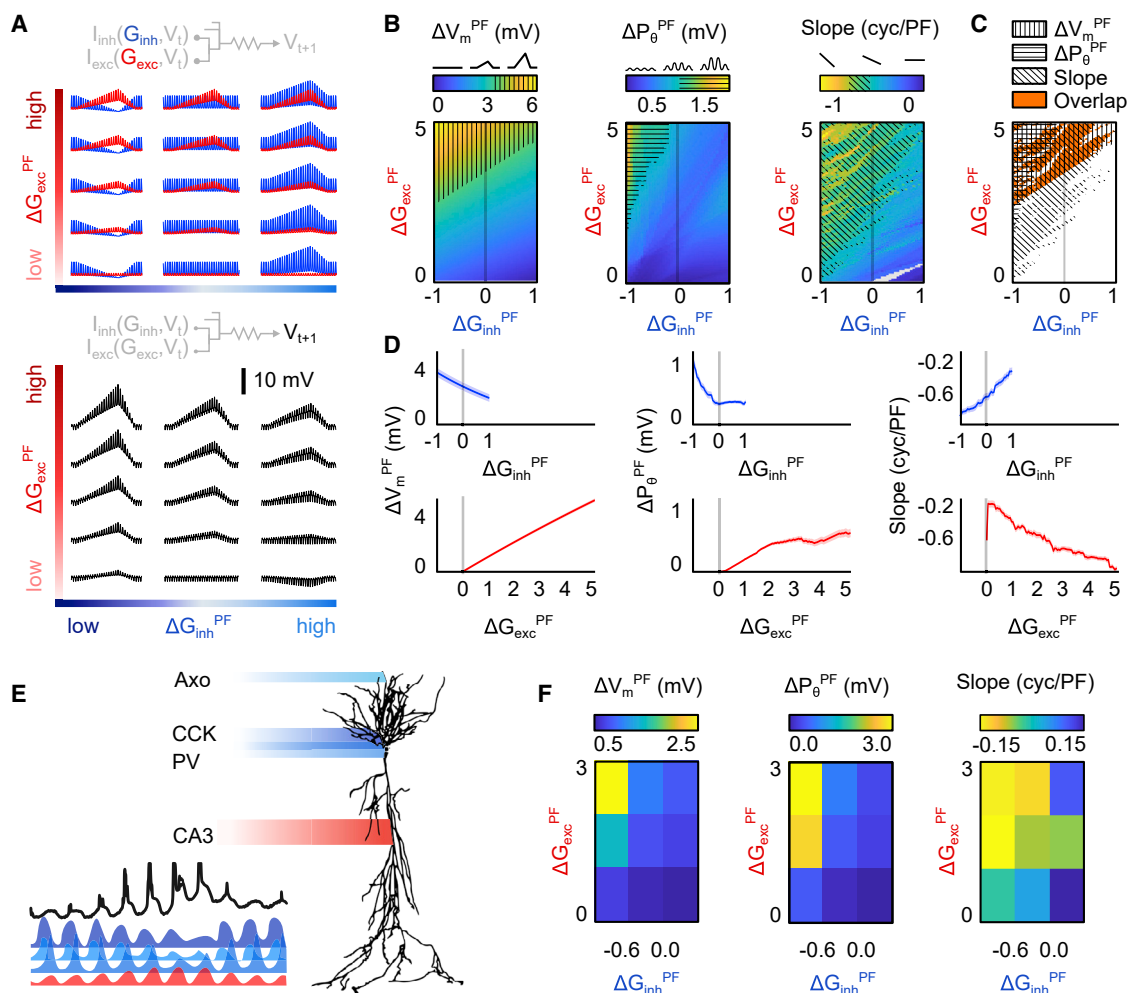


Figure 4. Modeling place field-tuned excitatory and inhibitory dynamics

(A) Place fields were simulated as a skewed modulation of G_{exc} and G_{inh} in the single-compartment passive model. Top, fifteen examples of all combinations obtained by co-varying excitation (from 0 to 5 folds at the place field peak, ΔG_{exc} , y axis) and inhibition (-1 to $+1$ folds at the place field peak, ΔG_{inh} , x axis). Bottom, resulting V_m .
(B) Place field peak amplitude (ΔV_m^{PF} , left), intracellular in-field/out-field theta power difference (ΔP_{θ}^{PF} , middle), and spike phase precession slope (right) values at different combinations of excitatory (y axis) and inhibitory (x axis) conductances. Observed experimental values (Table S1) are labeled with striped patterns.
(C) Superposition of ΔG_{inh} and ΔG_{exc} values that match the experimentally obtained values for ΔV_m^{PF} , ΔP_{θ}^{PF} , and phase precession slope. In orange, overlapping parameter regime across all three features.
(D) Average (mean \pm CI95) values of the three place field features considered (ΔV_m^{PF} , ΔP_{θ}^{PF} , and phase precession slope) as a function of ΔG_{inh} and ΔG_{exc} .
(E) Place field membrane potential dynamics in a realistic multi-compartment CA1 neuron model (Navas-Olive et al., 2020).
(F) Place field features; peak amplitude (ΔV_m^{PF} , left), intracellular in-field/out-field theta power difference (ΔP_{θ}^{PF} , middle), and spike phase precession slope for the realistic multi-compartment model.

et al., 2009) waveform of the theta-oscillating G_{inh} and G_{exc} (Figure 4A). We generated three classes (decreasing, constant, and increasing inhibition) of spatially tuned G_{exc} and G_{inh} curves by multiplying the basal theta dynamics (shown in Figures 2D and 3F, no holding current) with varying place modulated kernels (Figure S3D). Modulation of inhibition (ΔG_{inh}) and excitation (ΔG_{exc}) at the place field peak ranged from -1 - to $+1$ -fold and from 0 to 5-fold, respectively.

Whole-cell and extracellular recordings (Grienberger et al., 2017; Harvey et al., 2009; Lee et al., 2012; O'keefe and Recce, 1993) have identified three main signatures of place fields in

CA1 pyramidal cells: (1) ~ 6 mV depolarization at the place field peak (ΔV_m^{PF}) associated with increased firing rate; (2) $\sim 70\%$ increase of V_m theta power from baseline (ΔP_{θ}^{PF}), and (3) phase precession of the emitted spikes relative to the extracellularly recorded theta cycle (Table S1 and Figure 1C). To evaluate the relative contribution of ΔG_{exc} and ΔG_{inh} to these observed features, we quantified the three signatures (ΔV_m^{PF} , ΔP_{θ}^{PF} , and phase precession slope) for all place field simulations ($n = 101$ ΔG_{exc} steps, $n = 41$ ΔG_{inh} steps, $n = 4,141$ simulations), and displayed the effects on the 2D parametric heatmap where the y and x axes show the values of ΔG_{exc} and ΔG_{inh} , so that each

location of the heatmap represents a unique inhibitory-excitatory contribution to a particular feature of the place field (Figures 4B, 4C, and S3E).

In the simulations, place field amplitude (ΔV_{PF}) increased for both larger in-field upmodulation of the ΔG_{exc} and for decreasing ΔG_{inh} (Figures 4B–4D, left). Yet, both the intracellular theta power ($\Delta \theta$ power) and phase precession slope were more influenced by decreasing ΔG_{inh} than increasing ΔG_{exc} (Figures 4B and 4D, middle and right, Figure S3F). To ground these results, we compared the values obtained in our simulations with expected “target” values from our own and other’s previously published data (lattice areas in Figures 4B and 4C; Table S1 and Figures S3G and S3H). For all three signatures, relatively lower ΔG_{exc} values matched the experimental values when combined with moderate disinhibition (i.e., decrease of ΔG_{inh} ; Geiller et al., 2022; Valero et al., 2022). Moreover, by overlapping the regions of the three signatures that fitted the experimental values, we found that a combination of excitation ($\Delta G_{exc} \sim 2$ -fold) and reduced inhibition mimicked most closely the three place field signatures (Figure 4C, orange patches). This supports the hypothesis that the main features of CA1 place cell firing dynamics result from the competition of G_{exc} and G_{inh} . A similar combination of conductances was also a requirement to properly mimic the place field features in a biophysically more realistic neuron model (Navas-Olive et al., 2020), with multi-compartment CA1 pyramidal cell morphology, CA3 proximal dendritic excitatory and perisomatic PV, CCK, and axo-axonic GABAergic inputs (Figures 4E, 4F, and S4).

Testing model predictions by pharmacogenetic perturbation of inhibitory neurons

Our simulations predicted that appropriately coordinated excitation and disinhibition underlie place field properties (Royer et al., 2012). To test this hypothesis more directly, we experimentally manipulated inhibitory inputs on pyramidal neurons by combining pharmacogenetic and optogenetic methods. We virally expressed an “excitatory designer receptor exclusively activated by a designer drug” (Gq-DREADD) in all types of CA1 GABAergic interneurons by infusing Dlx5/6-Gq-DREADD adeno-associated virus (rAAV-hDLX) in the dorsal CA1 region of CamKII α -Cre:Ai32 freely moving mice ($n = 3$; Figure 5A; Rogers et al., 2021). Histological evaluation showed that virus infection successfully targeted CA1 interneurons in all sublayers (Figure 5B) (Dimidschstein et al., 2016).

As expected, clozapine N-oxide (CNO) activation of interneurons led to a strong suppression of pyramidal neuron spiking (68.35% with respect to DMSO; Figures 5C and S5A). Paradoxically, the firing rate of many interneurons also decreased (66.07% with respect to DMSO; Figures 5C and S5A). Such “paradoxical effects” have been described in the hippocampus (Rogers et al., 2021) and different cortical areas (Mahrach et al., 2020; Tsodyks et al., 1997) and were explained by the mutual inhibition of interneurons and the reduced excitatory inputs from the suppressed pyramidal cells. In addition to suppressing spontaneously occurring spikes in pyramidal neurons, we also found that their excitability in response to optogenetic stimulation decreased several folds after CNO injection (but not after DMSO vehicle injection; Figures 5D and S5B). Importantly,

this difference survived after normalizing for rate change (Figure S5B), indicating an increase in the local inhibitory transmission.

To examine the role of inhibition in place field signatures of pyramidal neurons, we exploited the position-dependent firing rate changes of interneurons. While interneurons rarely show *bona fide* single place fields, they do have characteristic tuning curves along the animal’s travel on the track that remain consistent across trials (Figure 5E; Souza et al., 2018; Valero et al., 2022; Wilson and McNaughton, 1993).

Mice ran on a linear track 100 min after the DMSO or CNO injection. The place-specific tuning patterns in interneurons were disrupted after Dlx-Gq DREADDs activation by CNO, as reflected by the decreased correlation of position-specific firing rates between control and CNO conditions compared with the effect of vehicle DMSO (Figures 5E and 5F). The altered spatially tuned features of interneurons after CNO were also demonstrated by the standard deviation of the firing maps (Figure 5G) and the mutual information between position and spiking activity (Figures 5H and S6). These changes could be dissociated from effects of the firing rates alone since even after downsampling of spikes in the DMSO condition the differences with CNO remained significant (see DMSO “resampled” in Figures 5G and 5H). Importantly, the altered spatial tuning of the inhibitory inputs (ΔG_{inh}) caused by Dlx-Gq DREADDs allowed for testing our model predictions on the three place field signatures discussed above: place field amplitude (ΔV_m^{PF}), in-field theta power change (ΔP_θ^{PF}), and phase precession slope (Figure 5I).

To examine the model predictions on the pyramidal cell population, we quantified the aforementioned place field properties. Place fields on the track for all place cells were sorted by the peak rate position before CNO (or DMSO) injection (Figures 6A and S5C). In line with the observed decrease of spatial modulation of interneurons, co-firing of pyramidal cells and interneurons was dampened around place fields during CNO (Figures S5D and S5E). As expected, both the standard deviation of the firing maps (Figure 6B), the in-field firing rates of pyramidal neurons (Figure 6C), and the difference between in-field and out-field firing (Figures S5F) decreased after CNO compared with DMSO injection, compatible with reduced place field amplitude (ΔV_m^{PF}), as predicted by the model. Mutual information between position and firing (Figures 6D and S6) and place field stability (Figure S5G) were also reduced, even beyond what was expected from the changes in the firing rate alone. We also observed a decrease in place field size, which could be explained by the overall decreased firing rate (Figure S5H).

As an indirect measure of the intracellular in-field theta power change (ΔP_θ^{PF}), we estimated the theta phase-locking of spikes (“mean vector length,” θ MVL) both in field and out field, and computed the in-field/out-field θ MVL log-ratio for all place fields. As expected from the larger intracellular V_m theta power in-field versus out-field (Grienberger et al., 2017; Harvey et al., 2009; Lee et al., 2012), theta phase locking of spikes (MVL) was stronger in field than out field in the intact animal resulting in ratios >1 (Figure 6E for DMSO). This in-field gain of MVL was reduced by CNO injection (Figure 6E), in line with our model prediction.

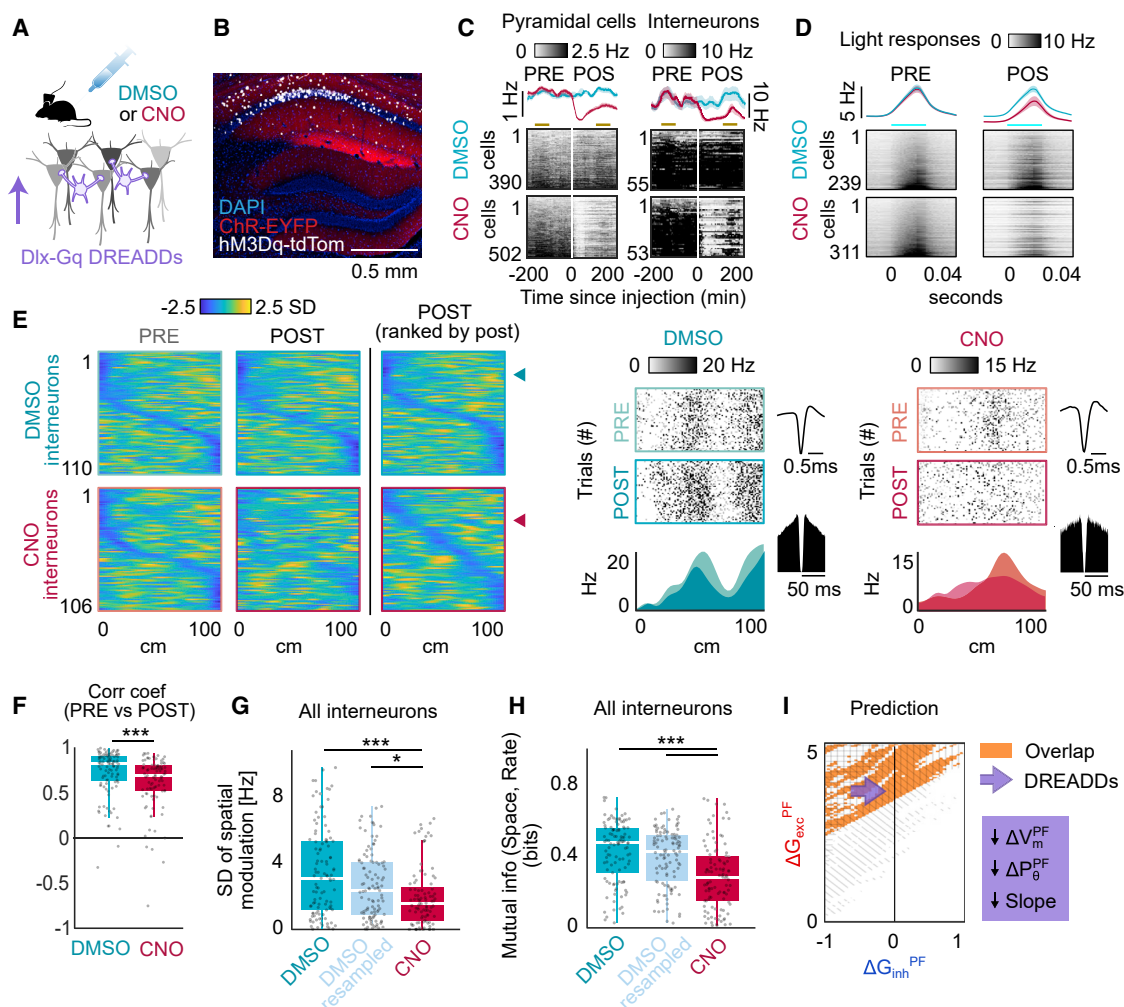


Figure 5. Chemogenetic activation of CA1 interneurons perturbs place field features

(A) Schematic of the combined chemogenetic/optogenetic manipulation experiments. CNO or DMSO (vehicle control) was intraperitoneally injected in CamKII α -Cre:Ai32 mice ($n = 3$) expressing the excitatory DREADD hM3Dq in all CA1 interneurons after AAV-hDlx virus injection.

(B) tdTomato-expressing DREADD interneurons (white) in CA1 layers and CamKII-ChR2-EYFP in pyramidal cells (red).

(C) Effect of CNO/DMSO injection (time 0) on the firing rate of pyramidal cells (left) and interneurons (right). Each row is the color-coded firing rate of a neuron. Orange lines show maze exploration epochs.

(D) Average peristimulus histograms (PSTH) of pyramidal cell responses to optogenetic stimulation (20 ms) before and after CNO or DMSO injection.

(E) Distribution of place-dependent firing rates on the track for all interneurons before and after DMSO (top, 110 fields from 55 interneurons) and CNO (bottom, 106 fields from 53 interneurons). Each field is a single row, sorted according to the location of their lowest Z scored rate. Middle and right panels, trial/track location raster plot for two representative interneurons (marked by triangles). Right insets, unit waveform and autocorrelogram.

(F) Place-dependent rate stability (Spearman's ρ) after injection for DMSO and CNO groups ($\chi^2_{1,204} = 16.23$, $p < 10^{-4}$, KW test).

(G) CNO decreases the standard deviation (SD) of the interneurons' rate maps. Differences persist after subsampling to match average rate between groups (DMSO resampled) ($\chi^2_{2,323} = 17.86$, $p < 10^{-3}$, KW test).

(H) Group differences of mutual information between location and firing rate ($\chi^2_{2,323} = 35.91$, $p < 10^{-7}$, KW test).

(I) In the model (see Figure 4C), reduction of the spatial modulation of interneurons (increase toward zero in the ΔG_{inh}^{PF} axis) predicts a decrease of the three place field signatures of pyramidal neurons shown in Figure 2 (ΔV_m^{PF} , ΔP_{θ}^{PF} , and phase precession slope). * $p < 0.05$, *** $p < 0.001$.

Finally, we found that the phase precession slope became less negative during CNO session (Figures 6F and 6G), a change that was independent of the concomitant firing rate reduction (Figures 6G and S5I, resampled). Consequently, mutual information between spatial position and theta phase of spiking, a measure of phase coding efficacy, was also decreased by CNO (Figure 6H).

In summary, in harmony with our model predictions and prior studies (Geiller et al., 2022; Royer et al., 2012; Valero et al., 2022), impairment of the spatial tuning of interneurons brought about by their pharmacogenetic perturbation resulted in reduced in-field firing, less in-field theta modulation of spiking (but not the overall θ MVL), and reduced slope of phase precession.

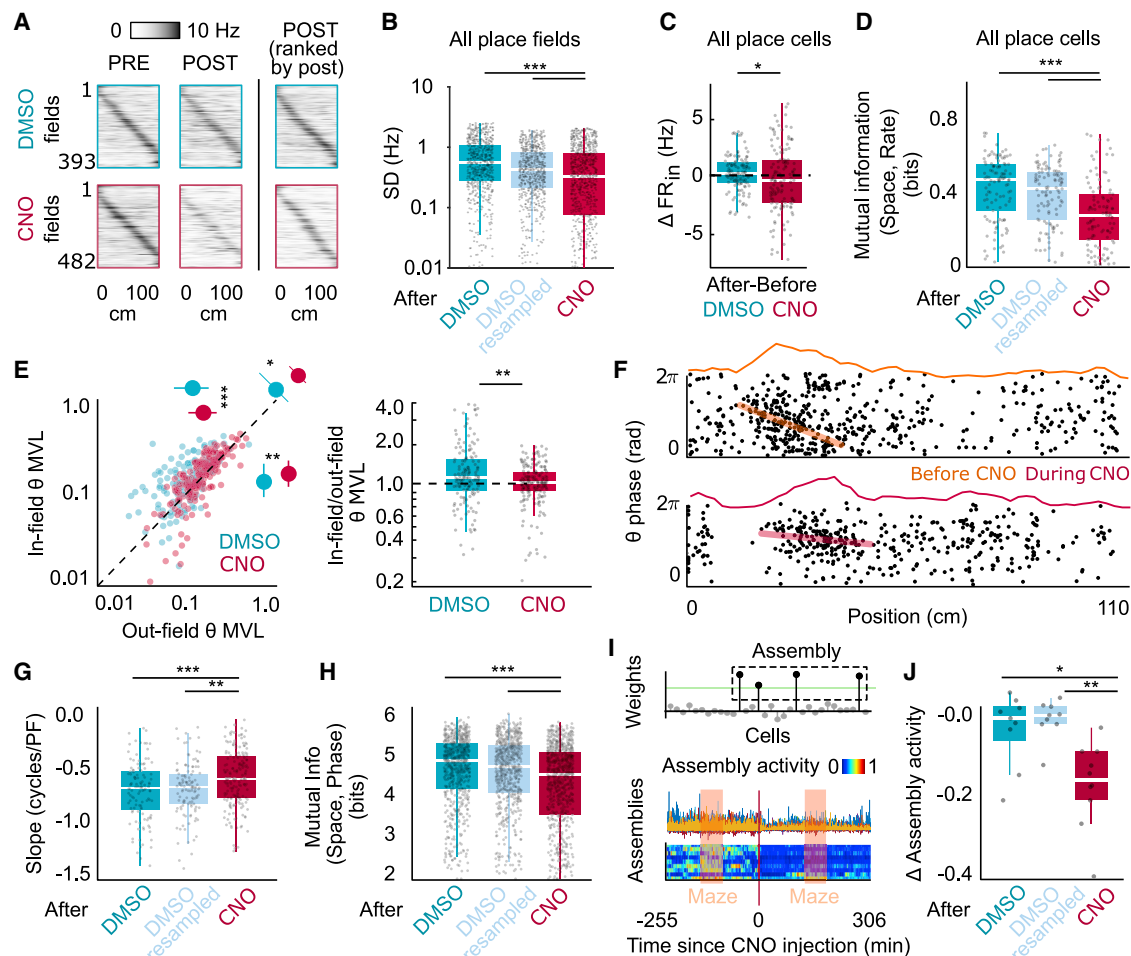


Figure 6. Perturbation of interneuron activity impairs place field features

(A) Rate maps of pyramidal cells before (PRE, left) and after (POST; middle) CNO (bottom) or DMSO (top) injection sorted by place field position in PRE (left panels). Right panels, place fields during CNO (bottom) or DMSO (top) sorted by POST.

(B) Standard deviation (SD) of firing maps after CNO or DMSO injection. CNO decreases SD ($\chi^2_{2,2236} = 87.72$, $p < 10^{-20}$, KW test).

(C) PRE-POST difference of in-field firing rate (ΔFR_{in}). CNO decreases in-field pyramidal cell firing rates ($\chi^2_{1,346} = 3.49$, $p = 0.045$, KW test).

(D) Mutual information between space and rate after DMSO and CNO injection. DMSO sessions were subsampled to match average rate between groups (DMSO resampled).

(E) Correlation between in-field and out-of-field theta mean vector length (MVL) after DMSO and CNO injections (in-field: $\chi^2_{1,346} = 7.07$, $p = 0.007$; out-field: $\chi^2_{1,346} = 38.41$, $p < 10^{-10}$, KW test; diagonal difference: $\chi^2_{1,346} = 6.11$, $p = 0.013$, KW test). The MVL ratio between in-field and out-of-field values is reduced by CNO (left panel; $\chi^2_{1,346} = 7.45$, $p = 0.006$, KW test).

(F) Spike theta phase precession of a representative CA1 place cell before (top) and after CNO administration (bottom). Each dot is a spike. The orange/red lines show phase-position correlation (“precession”) and spatial rate distribution.

(G) Phase precession slopes are less negative during CNO, compared with DMSO, and persist after downsampling spikes in DMSO condition ($\chi^2_{2,412} = 17.01$, $p = 0.0002$, KW test).

(H) Same display as in (G) for mutual information between space and phase ($\chi^2_{2,2337} = 58.63$, $p < 10^{-12}$, KW test).

(I) Top, relative weights of neurons for an example assembly. Z scored assembly activity before and after CNO injection for a representative session. Orange rectangles show epochs during track running.

(J) Assembly expression is reduced after CNO injection but not DMSO vehicle ($\chi^2_{2,25} = 12.83$, $p = 0.001$, KW test, $n = 3$ mice). * $p < 0.05$, ** $p < 0.01$.

Population level effects of interneuron perturbation

Theta phase coordination of spiking activity has been implicated in organizing cell assemblies as passing through consecutive place fields (Dragoi and Buzsáki, 2006; Harris et al., 2003; Petersen and Buzsáki, 2020; Skaggs et al., 1996). The critical role of local GABAergic interneuron activity in shaping phase precession dynamics suggests assembly expression should be also

affected. To test this prediction, we quantified the expression of CA1 neuronal assemblies (Lopes-dos-Santos et al., 2013) in 25-ms bins (Harris et al., 2003; Zutshi et al., 2022) before and during pharmacogenetic manipulation of interneurons (Figure 6I). As expected from the multiple impaired parameters of individual pyramidal neurons, CNO (but not DMSO) dramatically decreased the assembly expression (Figures 6I, 6J, S6C, and

S6D), independent of the reduced firing rates of pyramidal cells (Figure 6J; resampled).

DISCUSSION

Using intracellular recordings *in vivo* and fast-pulse optogenetic probing of hippocampal CA1 pyramidal cells, we found that excitation lags behind inhibition by approximately one-fifth of a theta cycle, and that G_{inh} dominates over G_{exc} across the entire cycle. In control conditions, the firing of intracellularly recorded cells occurred asymmetrically around the extracellular theta negativity with more spikes occurring on the ascending than on the descending phase, enabled by the relative level of G_{exc} over perisomatic G_{inh} . Tonic depolarization advanced the phase preference of spikes, producing a voltage-phase precession that spanned part of the theta cycle. These results were reproduced by both a single-compartment passive model endowed with the experimentally observed conductances and by a multi-compartment Hodgkin-Huxley type model. By adding a spatially modulated depolarizing signal coupled with decreased inhibition to the model, we found that the canonical place field features (a slow depolarization ramp, increased amplitude theta rhythmicity, and spike phase precession) emerged from the temporally coordinated increase of excitation and disinhibition. Consistently, DREADDs perturbation of GABAergic interneuron spiking interfered with the key place field features and changed coordinated assembly expression. Overall, our results demonstrate the necessity of both fast and slow temporal coordination of G_{inh} and G_{exc} for maintaining local circuit dynamics in the CA1 region.

Relationship between G_{inh} and G_{exc} affects theta oscillatory dynamics

While previous intracellular experiments have already provided insights on the role of perisomatic inhibition in theta oscillations (Grienberger et al., 2017; Harvey et al., 2009; Kamondi et al., 1998; Nuñez et al., 1990; Soltesz and Deschenes, 1993; Ylinen et al., 1995), our study was designed to clarify both the importance and the precise temporal/phase relationship between G_{inh} and G_{exc} . Within the theta cycle, G_{inh} peak was several times larger compared with G_{exc} , and G_{inh} preceded the peak of G_{exc} (Figure 2C). Both G_{exc} and G_{inh} peaked on the descending phase of the LFP theta waves, corresponding to the largest amplitude of slow gamma (30–80 Hz) oscillations (Fernández-Ruiz et al., 2017). The maximal firing from both upstream CA3 pyramidal cells (Mizuseki et al., 2009) and feed-forwardly activated perisomatic inhibitory neurons (i.e., CCK and PV basket cells and bistratified interneurons) also occur at this phase (Klausberger et al., 2005; Lapray et al., 2012; Valero and de la Prida, 2018; Viney et al., 2013). These circuit features may explain the asymmetry of theta waves (Buzsáki et al., 1985), as well as the uneven distribution of firing along the descending and ascending phases of theta (Belluscio et al., 2012; Navas-Olive et al., 2020; Skaggs et al., 1996).

Targeted manipulation of the somatic V_m in our intracellular experiments allowed us to examine how changes of G_{exc} and G_{inh} affected membrane polarity and firing preference relative to the extracellular LFP theta. Varying the holding potential from subthreshold to suprathreshold V_m levels led to a phase

reversal of intracellular theta waves at about -75 mV, which corresponds to the Cl^- equilibrium potential of GABA_A receptors (Borg-Graham et al., 1998; Ylinen et al., 1995). Another consequence of the depolarizing V_m was that spike threshold is reached at progressively earlier phases of the theta cycle (Kamondi et al., 1998; Magee, 2001). These experiments were complemented by short-pulse optogenetic probing of pyramidal cells in freely moving mice (Valero et al., 2022), which mimicked the effects of intracellular depolarization. Our computational models provided further support of the sufficiency of somatic G_{exc} and G_{inh} interplay. The simulations reproduced both subthreshold and spiking experimental results. Overall, these findings expand previous observations and provide support for the hypothesis that competition between G_{exc} and G_{inh} is an important component of theta oscillations.

G_{inh} - G_{exc} competition in place fields reproduces principal place cell features

The V_m -dependent spike phase advancement has been suggested to contribute to theta phase precession of spikes (Kamondi et al., 1998; Magee, 2001), although it is acknowledged that several inter-dependent mechanisms work in concert to achieve the predictive relationship between theta phase of spiking and the animal's position in the environment (Lisman, 2005; Maurer and McNaughton, 2007; O'Keefe and Recce, 1993). Our model simulations allowed examining this hypothesis (Figure 1B). Adding a slow depolarization, mimicking the postulated "place input" (O'Keefe and Nadel, 1978; Tsodyks et al., 1996), we could explore the various possible relationships between G_{inh} and G_{exc} and relate the simulations to the three major experimentally observed features of place fields, including the slow depolarization, increase of intracellular theta magnitude, and phase precession of spikes (Table S1). Of the large parameter space provided by the model, the best fit to experimental data was that in which a moderate level of place-field-related G_{exc} (Davoudi and Foster, 2019) was coupled with decreased G_{inh} (Geiller et al., 2022; Valero et al., 2022). Similar results were obtained by using a multi-compartment Hodgkin-Huxley CA1 neuron with theta-phase-specific inhibition by three different types of perisomatic interneurons. These combined simulations point to the key aspect of reduced within-field inhibition. The general view of place field mechanism is that a spatial input is conveyed to the hippocampus by way of the entorhinal cortex (Moser et al., 2014) and that place field are produced by an especially strong excitation of the distal dendrites of pyramidal cells (i.e., plateau potentials; Magee and Grienberger, 2020). Virtually all computational models, including ours, used an "added" spatial input, tacitly assuming a slow externally imposed excitation on the hippocampal networks (Grienberger et al., 2017; McClain et al., 2019; Tsodyks et al., 1996). In these models, inhibition is assumed to be "flat" (Grienberger et al., 2017) or to track the increased level of excitation ("balanced E/I models"; Bhatia et al., 2019).

In contrast to this "imposed" spatial input model, experiments have pointed out that hippocampal networks can maintain their own dynamics and cortical inputs simply create a new "initial condition" for internally generated sequential neuronal trajectories (Iltis et al., 2011). For example, when the animal is

required to hold memory about future goals, neuronal sequences with features indistinguishable from place cell sequences are recorded in the hippocampus (Eichenbaum, 2014; Mizumori et al., 1989; Pastalkova et al., 2008). When sparsely firing or “silent” hippocampal neurons are depolarized intracellularly or by optogenetic means, place fields instantaneously emerge (“unmasked”) in these neurons (Lee et al., 2012; Valero et al., 2022). Strong optogenetic discharge of neurons at a given spatial position can induce *bona fide* place fields but only if those neurons had already fired sporadically at that location (i.e., they had “ghost” fields; McKenzie et al., 2021; Valero et al., 2022). Thus, a large reservoir of representations may be actually stored in the subthreshold membrane dynamics (Valero et al., 2022).

The tacitly assumed requirement of specific spatial input for CA1 place field generation is further confronted by deafferentation experiments. After entorhinal or CA3 lesions or their local silencing, place fields persist in the hippocampus often with little or no change in firing rate, spike theta phase coupling, or the CA1 region’s ability to form coordinated place cell assemblies (Brun et al., 2002; Davoudi and Foster, 2019; Miao et al., 2015; Rueckemann et al., 2016; Schlesiger et al., 2018; Zutshi et al., 2022), although we cannot rule out residual activity in the experimentally manipulated areas. In addition to pyramidal cells, at least some types of interneurons often show a reliable position-firing relationship, an indication that transiently active neuronal assemblies dynamically engage their interneurons (Geisler et al., 2007; Marshall et al., 2002; Maurer et al., 2006), in agreement with our own results. Finally, altered inhibition is known to affect place field properties (Grienberger et al., 2017; Losonczy et al., 2010; Royer et al., 2012), and presynaptic interneurons of place cells have been shown to decrease their firing specifically within the place fields of place cells (Geiller et al., 2022), resulting in disinhibition of their target place cells (Valero et al., 2022). Potential sources of place-field-related interneuronal suppression include differential activation of mutually connected interneurons (Rogers et al., 2021) or interneuron-inhibiting vasoactive intestinal polypeptide (VIP) calretinin (CR) neurons, which can be activated by entorhinal inputs (Luo et al., 2020). An alternative mechanism is the retrograde suppression of the activity of perisomatic CCK interneurons by their bursting place cells (Freund, 2003).

Our simulations predicted an impairment of place field features just by altering inhibitory activity. In addition to decreasing the firing rates of place cells, DREADD chemogenetic activation of interneurons induced a “paradoxical” decrease of the overall activity of GABAergic interneurons. Several mechanisms can account for this effect, including shifting of dominant subgroups of highly active interneurons which transiently suppress the firing of both pyramidal cells and other interneurons (Mahrach et al., 2020; Rogers et al., 2021). Perturbation of the balanced interactions among interneurons altered their position tuning. In addition to these changes, our chemogenetic approach also affected within-field theta phase coupling and phase precession of place cells, decreasing their in-field gain and spatial information beyond what might be expected solely on firing rate changes.

Our findings support a framework of perpetually changing sequential activation of neurons within hippocampal networks. Under this model, preformed neuronal assemblies (Dragoi and

Tonegawa, 2010; McKenzie et al., 2021; Valero et al., 2022) continuously shift their activity, guided by short-term plasticity between interneurons and pyramidal cells, whose time course determines the “life time” of the currently active assembly (Kullmann et al., 2012). Assembly-recruited interneurons suppress competing groups, but because of the depressing nature of both E-I and I-E synapses (English et al., 2017), such transient suppression enables the maintenance of assembly sequences (Carrillo-Reid et al., 2015; Itskov et al., 2011; Pastalkova et al., 2008). In this new formulation, internal network organization provides the affordance of hippocampal networks to map external events onto their preexisting neuronal dynamics. An important role of external inputs may then be to select a new initial condition for the perpetually changing cell assemblies (“remapping”; Fernández-Ruiz et al., 2017; Muller and Kubie, 1987; Zutshi et al., 2022). Our experimental findings and model simulations add support to this view by demonstrating the key role of inhibitory conductance in place field activity.

Limitations of the study

We showed that the inhibitory inputs that control hippocampal CA1 pyramidal cells play an important role in the expression of place fields. Notwithstanding, the sources of inhibition in the hippocampus are highly heterogeneous (Klausberger et al., 2005), and previous works have shown that interneuronal diversity itself is an essential factor for theta generation (Bezaire et al., 2016; Klausberger et al., 2005; Navas-Olive et al., 2020) and spatial activity (Royer et al., 2012). Therefore, targeted manipulation of specific groups of interneurons will be an important task for future experiments by taking advantage of novel mouse recombinase driver lines (Valero et al., 2021).

STAR★METHODS

Detailed methods are provided in the online version of this paper and include the following:

- KEY RESOURCES TABLE
- RESOURCE AVAILABILITY
 - Lead contact
 - Material availability
 - Data and code availability
- EXPERIMENTAL MODEL AND SUBJECT DETAILS
- METHOD DETAILS
 - Intracellular recordings
 - Intracellular recording analysis
 - Uni-compartmental model
 - Biophysically realistic model
 - Extracellular recordings and behavior
 - Unit clustering and neuron classification
 - Place field and extracellular Spike-LFP coupling analysis
 - Assembly analysis
 - Histological processing and microscopy
- QUANTIFICATION AND STATISTICAL ANALYSIS
 - Statistical analysis

SUPPLEMENTAL INFORMATION

Supplemental information can be found online at <https://doi.org/10.1016/j.celrep.2022.111232>.

ACKNOWLEDGMENTS

We would like to thank T. Hainmueller, N. Nitzan, A. Fernandez-Ruiz, I. Zutshi, E. Cid, and the rest of the members of the Buzsáki and de la Prida laboratories for helpful comments on the project. This work was supported by the European Molecular Biology Organization (EMBO) postdoctoral fellowship (EMBO ALTF 1161–2017) and Human Frontiers Science Program (HFSP) postdoctoral fellowship (LT0000717/2018) to M.V., NIH grants (R01MH122391, U19NS104590, and U19NS107616) to G.B., and a grant from the Spanish Ministry of Science and Innovation MCIN/AEI/10.13039/501100011033 “ERDF A way of making Europe” (RTI2018-098581-B-I00) to L.M.P. A.N.O. is supported by a PhD fellowship (FPU17/03268) and by a short-term visit fellowship (EST19/00828) from the Spanish Ministry of Education.

AUTHOR CONTRIBUTIONS

Conceptualization, M.V., G.B., and L.M.P. Methodology: M.V., G.B., and L.M.P. Software: M.V. and A.N.O. Formal analysis: M.V. and A.N.O. Investigation: M.V. Data curation: M.V. Writing – original draft: M.V. and G.B. Writing – review & editing: all authors. Visualization: M.V. and A.N.O. Supervision: G.B., M.V., and L.M.P. Funding acquisition: G.B., L.M.P. and M.V.

DECLARATION OF INTERESTS

The authors declare no competing interests.

Received: May 4, 2022

Revised: June 30, 2022

Accepted: July 27, 2022

Published: August 23, 2022

REFERENCES

- Ahmed, O.J., and Mehta, M.R. (2009). The hippocampal rate code: anatomy, physiology and theory. *Trends Neurosci.* 32, 329–338. <https://doi.org/10.1016/j.tins.2009.01.009>.
- Andersen, P., Morris, R., Amaral, D., Bliss, T., and O'Keefe, J. (2009). *The Hippocampus Book* (Oxford University Press).
- Belluscio, M.A., Mizuseki, K., Schmidt, R., Kempter, R., and Buzsáki, G. (2012). Cross-frequency phase-phase coupling between θ and γ oscillations in the hippocampus. *J. Neurosci.* 32, 423–435. <https://doi.org/10.1523/JNEUROSCI.4122-11.2012>.
- Bezaire, M.J., Raikov, I., Burk, K., Vyas, D., and Soltesz, I. (2016). Interneuronal mechanisms of hippocampal theta oscillations in a full-scale model of the rodent CA1 circuit. *Elife* 5, e18566. <https://doi.org/10.7554/ELIFE.18566>.
- Bhatia, A., Moza, S., and Bhalla, U.S. (2019). Precise excitation-inhibition balance controls gain and timing in the hippocampus. *Elife* 8, e43415. <https://doi.org/10.7554/ELIFE.43415>.
- Borg-Graham, L.J., Monier, C., and Frégnac, Y. (1998). Visual input evokes transient and strong shunting inhibition in visual cortical neurons. *Nature* 393, 369–373. <https://doi.org/10.1038/30735>.
- Brun, V.H., Otnass, M.K., Molden, S., Steffenach, H.-A., Witter, M.P., Moser, M.-B., and Moser, E.I. (2002). Place cells and place recognition maintained by direct entorhinal-hippocampal circuitry. *Science* 296, 2243–2246. <https://doi.org/10.1126/science.1071089>.
- Burgess, N., Recce, M., and O'Keefe, J. (1994). A model of hippocampal function. *Neural Network* 7, 1065–1081. [https://doi.org/10.1016/S0893-6080\(05\)80159-5](https://doi.org/10.1016/S0893-6080(05)80159-5).
- Buzsáki, G., Leung, L.W., and Vanderwolf, C.H. (1983). Cellular bases of hippocampal EEG in the behaving rat. *Brain Res.* 287, 139–171.
- Buzsáki, G., Rappelsberger, P., and Kellényi, L. (1985). Depth profiles of hippocampal rhythmic slow activity ('theta rhythm') depend on behaviour. *Electroencephalogr. Clin. Neurophysiol.* 61, 77–88. [https://doi.org/10.1016/0013-4694\(85\)91075-2](https://doi.org/10.1016/0013-4694(85)91075-2).
- Carrillo-Reid, L., Lopez-Huerta, V.G., Garcia-Munoz, M., Theiss, S., and Arbuthnott, G.W. (2015). Cell assembly signatures defined by short-term synaptic plasticity in cortical networks. *Int. J. Neural Syst.* 25, 1550026. <https://doi.org/10.1142/S0129065715500264>.
- Chen, M. (2022). *Information Theory Toolbox*.
- Davoudi, H., and Foster, D.J. (2019). Acute silencing of hippocampal CA3 reveals a dominant role in place field responses. *Nat. Neurosci.* 22, 337–342. <https://doi.org/10.1038/s41593-018-0321-z>.
- Deuchars, J., and Thomson, A.M. (1996). CA1 pyramid-pyramid connections in rat hippocampus in vitro: dual intracellular recordings with biocytin filling. *Neuroscience* 74, 1009–1018. [https://doi.org/10.1016/0306-4522\(96\)00251-5](https://doi.org/10.1016/0306-4522(96)00251-5).
- Dimidschstein, J., Chen, Q., Tremblay, R., Rogers, S.L., Saldi, G.A., Guo, L., Xu, Q., Liu, R., Lu, C., Chu, J., et al. (2016). A viral strategy for targeting and manipulating interneurons across vertebrate species. *Nat. Neurosci.* 19, 1743–1749. <https://doi.org/10.1038/NN.4430>.
- Dragoi, G., and Buzsáki, G. (2006). Temporal encoding of place sequences by hippocampal cell assemblies. *Neuron* 50, 145–157. <https://doi.org/10.1016/j.neuron.2006.02.023>.
- Dragoi, G., and Tonegawa, S. (2010). Preplay of future place cell sequences by hippocampal cellular assemblies. *Nature* 469, 397–401. <https://doi.org/10.1038/nature09633>.
- Eichenbaum, H. (2014). Time cells in the hippocampus: a new dimension for mapping memories. *Nat. Rev. Neurosci.* 15, 732–744. <https://doi.org/10.1038/nrn3827>.
- English, D.F., McKenzie, S., Evans, T., Kim, K., Yoon, E., and Buzsáki, G. (2017). Pyramidal cell-interneuron circuit architecture and dynamics in hippocampal networks. *Neuron* 96, 505–520.e7. <https://doi.org/10.1016/j.neuron.2017.09.033>.
- Fernández-Ruiz, A., Oliva, A., Nagy, G.A., Maurer, A.P., Berényi, A., Buzsáki, G., Buzsáki, G., Groszmark, A., Mao, D., Mizuseki, K., et al. (2017). Entorhinal-CA3 dual-input control of spike timing in the Hippocampus by theta-gamma coupling. *Neuron* 93, 1213–1226.e5. <https://doi.org/10.1016/j.neuron.2017.02.017>.
- Fernández-Ruiz, A., Oliva, A., Soula, M., Rocha-Almeida, F., Nagy, G.A., Martín-Vázquez, G., and Buzsáki, G. (2021). Gamma rhythm communication between entorhinal cortex and dentate gyrus neuronal assemblies. *Science* 1979, eabf3119. <https://doi.org/10.1126/SCIENCE.ABF3119>.
- Freund, T.F. (2003). Interneuron Diversity series: rhythm and mood in perisomatic inhibition. *Trends Neurosci.* 26, 489–495. [https://doi.org/10.1016/S0166-2236\(03\)00227-3](https://doi.org/10.1016/S0166-2236(03)00227-3).
- Geiller, T., Sadeh, S., Rolotti, S.v., Blockus, H., Vancura, B., Negrean, A., Murray, A.J., Rózsa, B., Polleux, F., Clopath, C., and Losonczy, A. (2022). Local circuit amplification of spatial selectivity in the hippocampus. *Nature* 607, 105–109. <https://doi.org/10.1038/S41586-021-04169-9>.
- Geisler, C., Robbe, D., Zugaro, M., Sirota, A., and Buzsáki, G. (2007). Hippocampal place cell assemblies are speed-controlled oscillators. *Proc. Natl. Acad. Sci. USA* 104, 8149–8154. <https://doi.org/10.1073/PNAS.0610121104>.
- Grienberger, C., Milstein, A.D., Bittner, K.C., Romani, S., and Magee, J.C. (2017). Inhibitory suppression of heterogeneously tuned excitation enhances spatial coding in CA1 place cells. *Nat. Neurosci.* 20, 417–426. <https://doi.org/10.1038/nn.4486>.
- Groszmark, A.D., and Buzsáki, G. (2016). Diversity in neural firing dynamics supports both rigid and learned hippocampal sequences. *Science* 351, 1440–1443. <https://doi.org/10.1126/SCIENCE.AAD1935>.
- Hafting, T., Fyhn, M., Molden, S., Moser, M.-B., and Moser, E.I. (2005). Microstructure of a spatial map in the entorhinal cortex. *Nature* 436, 801–806. <https://doi.org/10.1038/nature03721>.

- Harris, K.D., Csicsvari, J., Hirase, H., Dragoi, G., and Buzsáki, G. (2003). Organization of cell assemblies in the hippocampus. *Nature* 424, 552–556. <https://doi.org/10.1038/nature01834>.
- Harvey, C.D., Collman, F., Dombeck, D.A., and Tank, D.W. (2009). Intracellular dynamics of hippocampal place cells during virtual navigation. *Nature* 461, 941–946. <https://doi.org/10.1038/nature08499>.
- Hasselmo, M.E., Bodelón, C., and Wyble, B.P. (2002). A proposed function for hippocampal theta rhythm: separate phases of encoding and retrieval enhance reversal of prior learning. *Neural Comput.* 14, 793–817. <https://doi.org/10.1162/089976602317318965>.
- Itskov, V., Curto, C., Pastalkova, E., and Buzsáki, G. (2011). Cell assembly sequences arising from spike threshold adaptation keep track of time in the Hippocampus. *J. Neurosci.* 31, 2828–2834. <https://doi.org/10.1523/JNEUROSCI.3773-10.2011>.
- Jensen, O., and Lisman, J.E. (2000). Position reconstruction from an ensemble of hippocampal place cells: contribution of theta phase coding. *J. Neurophysiol.* 83, 2602–2609. <https://doi.org/10.1152/JN.2000.83.5.2602>.
- Kamondi, A., Acsády, L., Wang, X.J., and Buzsáki, G. (1998). Theta oscillations in somata and dendrites of hippocampal pyramidal cells in vivo: activity-dependent phase-precession of action potentials. *Hippocampus* 8, 244–261. [https://doi.org/10.1002/\(SICI\)1098-1063](https://doi.org/10.1002/(SICI)1098-1063).
- Kanter, B.R., Lykken, C.M., Avesar, D., Weible, A., Dickinson, J., Dunn, B., Borgesius, N.Z., Roudi, Y., and Kentros, C.G. (2017). A novel mechanism for the grid-to-place cell transformation revealed by transgenic depolarization of medial entorhinal cortex layer II. *Neuron* 93, 1480–1492.e6. <https://doi.org/10.1016/J.NEURON.2017.03.001>.
- Klausberger, T., Marton, L.F., O'Neill, J., Huck, J.H.J., Dalezios, Y., Fuentelba, P., Suen, W.Y., Papp, E., Kaneko, T., Watanabe, M., et al. (2005). Complementary roles of cholecystokinin- and parvalbumin-expressing GABAergic neurons in hippocampal network oscillations. *J. Neurosci.* 25, 9782–9793. <https://doi.org/10.1523/JNEUROSCI.3269-05.2005>.
- Kullmann, D.M., Moreau, A.W., Bakiri, Y., and Nicholson, E. (2012). Plasticity of inhibition. *Neuron* 75, 951–962. <https://doi.org/10.1016/J.NEURON.2012.07.030>.
- Lapray, D., Laszotzci, B., Lagler, M., Viney, T.J., Katona, L., Valenti, O., Hartwich, K., Borhegyi, Z., Somogyi, P., and Klausberger, T. (2012). Behavior-dependent specialization of identified hippocampal interneurons. *Nat. Neurosci.* 15, 1265–1271. <https://doi.org/10.1038/nn.3176>.
- Latuske, P., Kornienko, O., Kohler, L., and Allen, K. (2018). Hippocampal remapping and its entorhinal origin. *Front. Behav. Neurosci.* 11, 253. <https://doi.org/10.3389/FNBEH.2017.00253/BIBTEX>.
- Lee, D., Lin, B.-J., and Lee, A.K. (2012). Hippocampal place fields emerge upon single-cell manipulation of excitability during behavior. *Science* 337, 849–853. <https://doi.org/10.1126/science.1221489>.
- Lai-Wo, S.L. (1984). Pharmacology of theta phase shift in the hippocampal CA1 region of freely moving rats. *Electroencephalogr. Clin. Neurophysiol.* 58, 457–466. [https://doi.org/10.1016/0013-4694\(84\)90142-1](https://doi.org/10.1016/0013-4694(84)90142-1).
- Lisman, J. (2005). The theta/gamma discrete phase code occurring during the hippocampal phase precession may be a more general brain coding scheme. *Hippocampus* 15, 913–922. <https://doi.org/10.1002/HIPO.20121>.
- Lopes-dos-Santos, V., Ribeiro, S., and Tort, A.B.L. (2013). Detecting cell assemblies in large neuronal populations. *J. Neurosci. Methods* 220, 149–166. <https://doi.org/10.1016/J.JNEUMETH.2013.04.010>.
- Losonczy, A., Zemelman, B.V., Vaziri, A., and Magee, J.C. (2010). Network mechanisms of theta related neuronal activity in hippocampal CA1 pyramidal neurons. *Nat. Neurosci.* 13, 967–972. <https://doi.org/10.1038/NN.2597>.
- Luo, X., Guet-McCreight, A., Villette, V., Francavilla, R., Marino, B., Chamberland, S., Skinner, F.K., and Topolnik, L. (2020). Synaptic mechanisms underlying the network state-dependent recruitment of VIP-expressing interneurons in the CA1 Hippocampus. *Cereb. Cortex* 30, 3667–3685. <https://doi.org/10.1093/CERCOR/BHZ334>.
- Magee, J.C. (2001). Dendritic mechanisms of phase precession in hippocampal CA1 pyramidal neurons. *J. Neurophysiol.* 86, 528–532. <https://doi.org/10.1152/JN.2001.86.1.528>.
- Magee, J.C., and Grienberger, C. (2020). Synaptic plasticity forms and functions. *Annu. Rev. Neurosci.* 43, 95–117. <https://doi.org/10.1146/ANNUREV-NEURO-090919-022842>.
- Mahrach, A., Chen, G., Li, N., van Vreeswijk, C., and Hansel, D. (2020). Mechanisms underlying the response of mouse cortical networks to optogenetic manipulation. *Elife* 9, e49967. <https://doi.org/10.7554/ELIFE.49967>.
- Marshall, L., Henze, D.A., Hirase, H., Leinekugel, X., Dragoi, G., and Buzsáki, G. (2002). Hippocampal pyramidal cell-interneuron spike transmission is frequency dependent and responsible for place modulation of interneuron discharge. *J. Neurosci.* 22, RC197. <https://doi.org/10.1523/JNEUROSCI.22-02-J0001.2002>.
- Maurer, A.P., and McNaughton, B.L. (2007). Network and intrinsic cellular mechanisms underlying theta phase precession of hippocampal neurons. *Trends Neurosci.* 30, 325–333. <https://doi.org/10.1016/J.TINS.2007.05.002>.
- Maurer, A.P., Cowen, S.L., Burke, S.N., Barnes, C.A., and McNaughton, B.L. (2006). Phase precession in hippocampal interneurons showing strong functional coupling to individual pyramidal cells. *J. Neurosci.* 26, 13485–13492. <https://doi.org/10.1523/JNEUROSCI.2882-06.2006>.
- McClain, K., Tingley, D., Heeger, D.J., and Buzsáki, G. (2019). Position-theta-phase model of hippocampal place cell activity applied to quantification of running speed modulation of firing rate. *Proc. Natl. Acad. Sci. USA* 116, 27035–27042. <https://doi.org/10.1073/PNAS.1912792116>.
- McKenzie, S., Huszár, R., English, D.F., Kim, K., Christensen, F., Yoon, E., and Buzsáki, G. (2021). Preexisting hippocampal network dynamics constrain optogenetically induced place fields. *Neuron* 109, 1040–1054.e7. <https://doi.org/10.1016/J.NEURON.2021.01.011>.
- Miao, C., Cao, Q., Ito, H.T., Yamahachi, H., Witter, M.P., Moser, M.B., and Moser, E.I. (2015). Hippocampal remapping after partial inactivation of the medial entorhinal cortex. *Neuron* 88, 590–603. <https://doi.org/10.1016/J.NEURON.2015.09.051>.
- Milstein, A.D., Li, Y., Bittner, K.C., Grienberger, C., Soltesz, I., Magee, J.C., and Romani, S. (2021). Bidirectional synaptic plasticity rapidly modifies hippocampal representations. *Elife* 10, e73046. <https://doi.org/10.7554/ELIFE.73046>.
- Mizumori, S.J., McNaughton, B.L., Barnes, C.A., and Fox, K.B. (1989). Preserved spatial coding in hippocampal CA1 pyramidal cells during reversible suppression of CA3c output: evidence for pattern completion in hippocampus. *J. Neurosci.* 9, 3915–3928.
- Mizuseki, K., Sirota, A., Pastalkova, E., and Buzsáki, G. (2009). Theta oscillations provide temporal windows for local circuit computation in the entorhinal-hippocampal loop. *Neuron* 64, 267–280. <https://doi.org/10.1016/j.neuron.2009.08.037>.
- Mizuseki, K., Diba, K., Pastalkova, E., and Buzsáki, G. (2011). Hippocampal CA1 pyramidal cells form functionally distinct sublayers. *Nat. Neurosci.* 14, 1174–1181. <https://doi.org/10.1038/nn.2894>.
- Moser, E.I., Roudi, Y., Witter, M.P., Kentros, C., Bonhoeffer, T., and Moser, M.B. (2014). Grid cells and cortical representation. *Nat. Rev. Neurosci.* 15, 466–481. <https://doi.org/10.1038/NRN3766>.
- Muller, R.U., and Kubie, J.L. (1987). The effects of changes in the environment on the spatial firing of hippocampal complex-spike cells. *J. Neurosci.* 7, 1951–1968. <https://doi.org/10.1523/JNEUROSCI.07-07-01951.1987>.
- Muller, R.U., and Kubie, J.L. (1989). The firing of hippocampal place cells predicts the future position of freely moving rats. *J. Neurosci.* 9, 4101–4110. <https://doi.org/10.1523/JNEUROSCI.09-12-04101.1989>.
- Navas-Olive, A., Valero, M., Jurado-Parras, T., de Salas-Quiroga, A., Averkin, R.G., Gambino, G., Cid, E., and de la Prida, L.M. (2020). Multimodal determinants of phase-locked dynamics across deep-superficial hippocampal sublayers during theta oscillations. *Nat. Commun.* 11, 2217. <https://doi.org/10.1038/s41467-020-15840-6>.

- Núñez, A., García-Austt, E., and Buño, W. (1990). Slow intrinsic spikes recorded in vivo in rat CA1–CA3 hippocampal pyramidal neurons. *Exp. Neurol.* 109, 294–299. [https://doi.org/10.1016/S0014-4886\(05\)80020-2](https://doi.org/10.1016/S0014-4886(05)80020-2).
- O'Keefe, J., and Recce, M.L. (1993). Phase relationship between hippocampal place units and the EEG theta rhythm. *Hippocampus* 3, 317–330.
- O'Keefe, J., and Nadel, L. (1978). *The hippocampus as a Cognitive Map* (Clarendon Press).
- Pastalkova, E., Itskov, V., Amarasingham, A., and Buzsáki, G. (2008). Internally generated cell assembly sequences in the rat Hippocampus. *Science* 321, 1322–1327. <https://doi.org/10.1126/science.1159775>.
- Petersen, P.C., and Buzsáki, G. (2020). Cooling of medial septum reveals theta phase lag coordination of hippocampal cell assemblies. *Neuron* 107, 731–744.e3. <https://doi.org/10.1016/J.NEURON.2020.05.023>.
- Petersen, P.C., Vestergaard, M., Jensen, K.H.R., and Berg, R.W. (2014). Pre-motor spinal network with balanced excitation and inhibition during motor patterns has high resilience to structural division. *J. Neurosci.* 34, 2774–2784. <https://doi.org/10.1523/JNEUROSCI.3349-13.2014>.
- Petersen, P.C., Siegle, J.H., Steinmetz, N.A., Mahallati, S., and Buzsáki, G. (2021). CellExplorer: a framework for visualizing and characterizing single neurons. *Neuron* 109, 3594–3608.e2. <https://doi.org/10.1016/J.NEURON.2021.09.002>.
- Rogers, S., Rozman, P.A., Valero, M., Doyle, W.K., and Buzsáki, G. (2021). Mechanisms and plasticity of chemogenically induced interneuronal suppression of principal cells. *Proc. Natl. Acad. Sci. USA* 118, e2014157118. <https://doi.org/10.1073/PNAS.2014157118>.
- Rolls, E.T., Stringer, S.M., and Elliot, T. (2006). Entorhinal cortex grid cells can map to hippocampal place cells by competitive learning. *Network* 17, 447–465. <https://doi.org/10.1080/09548980601064846>.
- Royer, S., Zemelman, B. v., Losonczy, A., Kim, J., Chance, F., Magee, J.C., and Buzsáki, G. (2012). Control of timing, rate and bursts of hippocampal place cells by dendritic and somatic inhibition. *Nat. Neurosci.* 15, 769–775. <https://doi.org/10.1038/nn.3077>.
- Rueckemann, J.W., Dimauro, A.J., Rangel, L.M., Han, X., Boyden, E.S., and Eichenbaum, H. (2016). Transient optogenetic inactivation of the medial entorhinal cortex biases the active population of hippocampal neurons. *Hippocampus* 26, 246–260. <https://doi.org/10.1002/HIPO.22519>.
- Savelli, F., and Knierim, J.J. (2010). Hebbian analysis of the transformation of medial entorhinal grid-cell inputs to hippocampal place fields. *J. Neurophysiol.* 103, 3167–3183. <https://doi.org/10.1152/JN.00932.2009>.
- Schlesiger, M.I., Boubil, B.L., Hales, J.B., Leutgeb, J.K., and Leutgeb, S. (2018). Hippocampal global remapping can occur without input from the medial entorhinal cortex. *Cell Rep.* 22, 3152–3159. <https://doi.org/10.1016/J.CELREP.2018.02.082>.
- Skaggs, W.E., McNaughton, B.L., Wilson, M.A., and Barnes, C.A. (1996). Theta phase precession in hippocampal neuronal populations and the compression of temporal sequences. *Hippocampus* 6, 6149–6172. [https://doi.org/10.1002/\(SICI\)1098-1063\(1996\)6:2](https://doi.org/10.1002/(SICI)1098-1063(1996)6:2).
- Solstad, T., Moser, E.I., and Einevoll, G.T. (2006). From grid cells to place cells: a mathematical model. *Hippocampus* 16, 1026–1031. <https://doi.org/10.1002/HIPO.20244>.
- Soltész, I., and Deschênes, M. (1993). Low- and high-frequency membrane potential oscillations during theta activity in CA1 and CA3 pyramidal neurons of the rat hippocampus under ketamine-xylazine anesthesia. *J. Neurophysiol.* 70, 97–116. <https://doi.org/10.1152/JN.1993.70.1.97>.
- Souza, B.C., Pavão, R., Belchior, H., and Tort, A.B.L. (2018). On information metrics for spatial coding. *Neuroscience* 375, 62–73. <https://doi.org/10.1016/J.NEUROSCIENCE.2018.01.066>.
- Steffenach, H.A., Witter, M., Moser, M.B., and Moser, E.I. (2005). Spatial memory in the rat requires the dorsolateral band of the entorhinal cortex. *Neuron* 45, 301–313. <https://doi.org/10.1016/J.NEURON.2004.12.044>.
- Tsodyks, M. v., Skaggs, W.E., Sejnowski, T.J., and McNaughton, B.L. (1996). Population dynamics and theta rhythm phase precession of hippocampal place cell firing: a spiking neuron model. *Hippocampus* 6, 271–280. [https://doi.org/10.1002/\(SICI\)1098-1063\(1996\)6:3](https://doi.org/10.1002/(SICI)1098-1063(1996)6:3).
- Tsodyks, M.v., Skaggs, W.E., Sejnowski, T.J., and McNaughton, B.L. (1997). Paradoxical effects of external modulation of inhibitory interneurons. *J. Neurosci.* 17, 4382–4388. <https://doi.org/10.1523/JNEUROSCI.17-11-04382.1997>.
- Valero, M., and de la Prida, L.M. (2018). The hippocampus in depth: a sublayer-specific perspective of entorhinal-hippocampal function. *Curr. Opin. Neurobiol.* 52, 107–114. <https://doi.org/10.1016/j.conb.2018.04.013>.
- Valero, M., Cid, E., Averkin, R.G., Aguilar, J., Sanchez-Aguilera, A., Viney, T.J., Gomez-Dominguez, D., Bellistri, E., and de la Prida, L.M. (2015). Determinants of different deep and superficial CA1 pyramidal cell dynamics during sharp-wave ripples. *Nat. Neurosci.* 18, 1281–1290. <https://doi.org/10.1038/nn.4074>.
- Valero, M., Averkin, R.G., Fernandez-Lamo, I., Aguilar, J., Lopez-Pigozzi, D., Brotons-Mas, J.R., Cid, E., Tamas, G., Menendez de la Prida, L., Prida, L.M., et al. (2017). Mechanisms for selective single-cell reactivation during offline sharp-wave ripples and their distortion by fast ripples. *Neuron* 94, 1234–1247.e7. <https://doi.org/10.1016/j.neuron.2017.05.032>.
- Valero, M., Viney, T.J., Machold, R., Mederos, S., Zutshi, I., Schuman, B., Senzai, Y., Rudy, B., and Buzsáki, G. (2021). Sleep down state-active ID2/Nkx2.1 interneurons in the neocortex. *Nat. Neurosci.* 24, 401–411. <https://doi.org/10.1038/s41593-021-00797-6>.
- Valero, M., Zutshi, I., Yoon, E., and Buzsáki, G. (2022). Probing subthreshold dynamics of hippocampal neurons by pulsed optogenetics. *Science* 375, 570–574. <https://doi.org/10.1126/SCIENCE.ABM1891>.
- Viney, T.J., Laszotz, B., Katona, L., Crump, M.G., Tukker, J.J., Klausberger, T., and Somogyi, P. (2013). Network state-dependent inhibition of identified hippocampal CA3 axo-axonic cells in vivo. *Nat. Neurosci.* 16, 1802–1811. <https://doi.org/10.1038/nn.3550>.
- Wilson, M.A., and McNaughton, B.L. (1993). Dynamics of the hippocampal ensemble code for space. *Science* 261, 1055–1058. <https://doi.org/10.1126/SCIENCE.8351520>.
- Wu, F., Stark, E., Ku, P.C., Wise, K.D., Buzsáki, G., and Yoon, E. (2015). Monolithically Integrated μ LEDs on Silicon Neural Probes for High-Resolution Optogenetic Studies in Behaving Animals. *Neuron* 88, 1136–1148. <https://doi.org/10.1016/j.neuron.2015.10.032>.
- Ylinen, A., Soltész, I., Bragin, A., Penttonen, M., Sik, A., and Buzsáki, G. (1995). Intracellular correlates of hippocampal theta rhythm in identified pyramidal cells, granule cells, and basket cells. *Hippocampus* 5, 78–90. <https://doi.org/10.1002/hipo.450050110>.
- Zutshi, I., Valero, M., Fernández-Ruiz, A., and Buzsáki, G. (2022). Extrinsic control and intrinsic computation in the hippocampal CA1 circuit. *Neuron* 110, 658–673.e5. <https://doi.org/10.1016/J.NEURON.2021.11.015>.

STAR★METHODS

KEY RESOURCES TABLE

REAGENT or RESOURCE	SOURCE	IDENTIFIER
Antibodies		
Mouse anti-calbindin D-28k	Swant	Cat# 300; RRID: AB_10000347
Rhodamine Red goat anti-mouse IgG	Thermo Fisher	Cat# 115-295-003; RRID: AB_2338756
Alexa Fluor488-conjugated streptavidin	Jackson ImmunoResearch	Cat# 016-540-084; RRID: AB_2337249
Bacterial and virus strains		
pAAV-hDlx-GqDREADD-dTomato-Fishell-4	addgene	83897-AAV1
Chemicals, peptides, and recombinant proteins		
Neurobiotin tracer	Vector Labs	Cat# SP-1120
DPX mountant	VWR	360294H
DAPI (4',6-Diamidino-2-Phenylindole, Dihydrochloride)	Thermo Fisher	D1306
C&B Metabond	Parkell	Cat#S380
Clozapine N-oxide hydrochloride	Sigma-Aldrich	SML2304
Experimental models: Organisms/strains		
Mouse: B6.Cg-Tg(Camk2a-cre)T29-1St/J	Jackson Laboratory	RRID:IMSR_JAX:005359
Mouse: B6; 129S-Gt(ROSA)26Sortm32 (CAG-COP4*H134R/EYFP)Hze/J	Jackson Laboratory	RRID:IMSR_JAX:012569
Rat: Wistar	Instituto Cajal Animal facility	N/A
Software and algorithms		
HippoCookBook toolbox (MATLAB toolbox for extracellular/intracellular recordings and behaviour)	Manuel Valero	https://github.com/cortex-lab/KiloSort (https://doi.org/10.5281/zenodo.6902376)
LCN-HippoModel (python-based biophysically realistic model)	Andrea Navas-Olive and de la Prida lab	https://github.com/PridaLab/LCN-HippoModel (https://doi.org/10.5281/zenodo.6902418)
KiloSort (template-based spike sorting MATLAB software)	Pachitariu M & Cortex-lab	https://github.com/cortex-lab/KiloSort
KilosortWrapper	Peter C. Petersen & Brendon Watson	https://github.com/petersenpeter/KilosortWrapper
Phy (Python GUI for manual spike curation)	Cyrille Rossant, Ken Harris et al.	https://github.com/cortex-lab/phy
Phy plugins	Peter C. Petersen	https://github.com/petersenpeter/phy1-plugins
MATLAB	MathWorks	https://www.mathworks.com/
FMA Toolbox (MATLAB toolbox for Freely Moving Animal (FMA))	Michael Zugaro	https://fmatoolbox.sourceforge.net/
CellExplorer (Cell classification pipeline and graphical interface)	Petersen and Buzsáki, 2020	https://linkinghub.elsevier.com/retrieve/pii/S0896627321006565
Other		
Silicon probes	Neuronexus, Cambridge Neurotech	A1x16, H3
4 shank μ LED probes	Plexon	NeuroLight Optoelectrode
RHD2000 USB Interface Board	Intan Technologies	C3100
64 and 32 channel digital amplifiers	Intan Technologies	C3314, C3324
PulsePal v2	Sanworks	N/A
Axoclamp 900A Microelectrode Amplifier	Molecular Devices	N/A
Data acquisition interface Power3A	Cambridge Electronic Design Limited (CED)	Power1401-3A
3D printed microdrives	Mihály Vöröslakos, Peter Petersen and György Buzsáki	https://github.com/buzsakilab/3d_print_designs

RESOURCE AVAILABILITY

Lead contact

Further information and requests for resources and reagents should be directed to and will be fulfilled by the lead contact, György Buzsáki (gyorgy.buzsaki@nyumc.org).

Material availability

This study did not generate new unique reagents.

Data and code availability

- The data for this study is publicly available in the Buzsáki Lab Databank: <https://buzsakilab.com/wp/public-data/> (extracellular recording dataset and intracellular recording in head-fixed mice dataset) or is available upon request from the [lead contact](#) (intracellular recording in anesthetized rats).
- All custom code for preprocessing and analyzing the data can be found on <https://github.com/valegarman/HippoCookBook> (Zenodo: 6902376; <https://doi.org/10.5281/zenodo.6902376>). The code for the biophysically realistic model is publicly available at <https://github.com/PridaLab/LCN-HippoModel/tree/place-field> (Zenodo: 6902418; <https://doi.org/10.5281/zenodo.6902418>). All original code has been deposited at Zenodo and is publicly available as of the date of publication. DOIs are listed in the [key resources table](#).
- Any additional information required to reanalyze the data reported in this paper is available from the [lead contact](#) upon request.

EXPERIMENTAL MODEL AND SUBJECT DETAILS

All experiments were approved by the Institutional Animal Care and Use Committee (IACUC) at New York University Medical Center and the Ethics Committee of the Instituto Cajal (CSIC). Intracellular recordings in anesthetized rats were obtained in Madrid and were performed according to the Spanish legislation (R.D. 1201/2005 and L.32/2007), the European Communities Council Directives of 1986 (86/609/EEC) and 2003 (2003/65/CE) for animal research. All animals were kept in the vivarium on a 12-h light/dark cycle and were housed 2–3 per cage. Following surgery, the mice were moved to a 12-hour reverse light cycle (lights on/off at 7 pm/am) and housed individually. Prior to behavior training, mice were provided food and water ad libitum, but were water restricted to maintain 85% of their weight during and after behavioral training. Homozygous CaMKIIa-Cre line T29-1 transgenic mice (Jackson Laboratory #005359) were crossed with homozygous Ai32 mice (Jackson Laboratory #012569) to express channelrhodopsin2 (ChR2) in neurons expressing CaMKIIa in F1 hybrid mice. We used $n = 7$ male F1 hybrid mice ($n = 3$ mice for extracellular recordings and $n = 4$ for intracellular recordings in head-fixed conditions; 25–40 g, 30–50 weeks of age) and $n = 10$ male and female Wistar rats (240–450 gr; 20 to 50 weeks of age).

METHOD DETAILS

Intracellular recordings

For intracellular recordings in head-fixed mice, mice were implanted with titanium head plates ([English et al., 2017](#)) above the frontal bones, and 50- μ m stainless steel ground wire between the skull and dura over the cerebellum. A \sim 200 μ m diameter craniotomy was made, and the dura was removed above dorsal hippocampus (antero-posterior 2.0 mm, mediolateral 1.5 mm). The craniotomy was covered with Kwik-Sil (World Precision Instruments) until the day of recording. Mice were habituated to head fixation over one week and were allowed to run on top of a 15 cm diameter wheel during fixation. On the day of recording, the Kwik-Sil was removed, and sharp pipettes were pulled from 1.5 mm/0.86 mm outer/inner diameter borosilicate glass (A-M Systems) on a Flaming-Brown puller (Sutter Instruments) and filled with 1.5 M potassium acetate and 2% Neurobiotin (wt/vol, Vector Labs). *In vivo* pipette impedances varied from 40–90 M Ω . Intracellular recording were performed blindly and the micropipette was driven by a robotic manipulator (Sutter MP-285). Signals were acquired with an intracellular amplifier (Axoclamp 900A) at 100 \times gain.

The dataset of urethane anesthetized rats was collected and used previously ([Valero et al., 2015, 2017](#)). Briefly, rats were anesthetized with urethane (1.2 g per kg of body weight, intraperitoneal) and fastened to the stereotaxic frame. Body temperature was kept constant at 37 $^{\circ}$. A window of \sim 2 mm diameter was drilled above the right hippocampus for CA1 (AP: -3.7 mm; ML: 3 mm), and the dura was gently removed to allow electrode penetration. For intracellular recording and labeling, sharp pipettes were pulled from 1.5 mm/0.86 mm outer/inner diameter borosilicate glass (A-M Systems) on a Flaming-Brown puller (Sutter Instruments) and filled with 1.5 M potassium acetate and 2% Neurobiotin (wt/vol, Vector Labs). *In vivo* pipette impedances varied from 50–100 M Ω . Intracellular recordings were obtained blindly, driven by a hydraulic manipulator (Narishige). Signals were acquired with an intracellular amplifier (Axoclamp 900A) at 100 \times gain. Before recordings started, the craniotomy was covered by 3% agar to improve stability.

Intracellular recording analysis

Cells with intracellular action potential amplitude smaller than 40 mV in response to depolarizing current pulses of 0.3 nA amplitude were excluded. The resting membrane potential and input resistance were estimated by linear regression between baseline potential data and the associated holding current using custom-made code (<https://github.com/valegarman/HippoCookBook>). For phase analysis of synaptic changes during theta, we adopted the general method of Borg-Graham (Borg-Graham et al., 1998; Valero et al., 2017).

Briefly, membrane potential deflections at phase bin (3.6 deg) were plotted against the holding current (V_{hold}) and fit linearly to extract the reversal potential, $V_{rev}(\text{phase})$ and the total conductance, $G(\text{phase})$, as the intersection point with the abscissa's axis and the slope of the linear regression, respectively (Petersen et al., 2014; Valero et al., 2017):

$$G_{inh + exc}(\text{phase}) = \frac{V_{hold}}{\frac{\Delta V_m(\text{phase})}{R} \cdot m}$$

From the total conductance ($G_{Total}(\text{phase}) = G_{inh}(\text{phase}) + G_{exc}(\text{phase}) - G_{leak}$) we finally estimated the excitatory and inhibitory conductances by the GABAergic and glutamatergic reversal potential ($E_{GABAa} = -80$ mV and $E_{Glutamate} = 0$ mV) as follow:

$$G_{inh}(\text{phase}) = G_{Total} \cdot \frac{E_{Glutamate} - V_{Rev}}{E_{Glutamate} - E_{GABAa}}$$

and

$$G_{exc}(\text{phase}) = G_{Total} \cdot \frac{E_{GABAa} - V_{Rev}}{E_{Glutamate} - E_{GABAa}}$$

The theta-band phase of the LFP recorded at the highest theta power channel above CA1 stratum pyramidale was estimated as the Hilbert transform of the narrowband filtered LFP (3–7 Hz for anesthetized conditions). Theta epochs were detected automatically using the ratio of the power in theta band to the power of nearby bands (1–3 Hz, 12–14 Hz) of CA1 LFP. Theta peaks correspond 0 rad (0 deg) and 2π rad (360 deg) and troughs at π rad (180 deg) and 3π rad (540 deg) of theta waves throughout the manuscript. Theta modulation indices for each neuron were calculated using the mean resultant length of the phases, and significance was estimated using the Rayleigh test for non-uniformity. The mean angle and mean resultant length of the theta phases for a given neuron's spikes were taken as the preferred phase and modulation strength of that neuron respectively.

Uni-compartmental model

Our objective was to have a conceptual model of input integration, so we opted for a simple uni-compartmental model, composed by a membrane resistance of $R_m = 5.38$ M Ω , and four different input currents: leakage current (I_{leak}), defined as:

$$I_{leak}(t) = \frac{-1}{R_m} (V_{mem}(t) - V_{rest})$$

where $V_{mem}(t)$ is membrane potential at time t , and resting membrane potential was defined as $V_{rest} = -65$ mV; excitatory (I_{exc}) and inhibitory (I_{inh}) currents, which followed:

$$I_{exc}(t) = -G_{exc}(t) \cdot (V_{mem}(t) - V_{exc}^{rev})$$

$$I_{inh} = -G_{inh}(t) \cdot (V_{mem}(t) - V_{inh}^{rev})$$

where $G_{exc}(t)$ and $G_{inh}(t)$ represented experimental global excitatory and inhibitory conductances, and $V_{exc}^{rev} = -15$ mV and $V_{inh}^{rev} = -75$ mV; and holding current (I_{hold}), which were constant along time, and to target specific holding potentials (from -100 mV to -30 mV). We simulated them as:

$$I_{hold} = \frac{-1}{R_m} (V_{hold} - V_{rest})$$

Membrane potential was updated following:

$$\begin{aligned} I_{total}(t) &= I_{exc}(t) + I_{inh}(t) + I_{leak}(t) + I_{hold} \\ V_{mem}(t+1) &= V_{mem}(t) + R_m \cdot I_{total}(t) \end{aligned}$$

Conductance dynamics for each theta cycle were modeled as double exponential functions (exp2syn):

$$\text{exp2syn}(\theta, \varphi_1, \varphi_2) = \exp(-\theta / \varphi_2) - \exp(-\theta / \varphi_1)$$

being $\theta \in (0, 360)$ theta phases, and $\varphi_1 = 180$ deg and $\varphi_2 = 181$ deg raise and decay constants. This was circularly shifted by $\varphi_{circ}^{inh} = 240$ deg and $\varphi_{circ}^{exc} = 280$ deg. A final G_{base} was obtained by applying two consecutive moving averaging windows of 40 deg to smooth dynamics and normalizing it to range from 0 to 1. With this $G_{base}(t)$, $G_{exc}(t)$ and $G_{inh}(t)$ were defined as:

$$G(t) = G_{\min} + (G_{\max} - G_{\min}) \cdot G_{\text{base}}(t)$$

where $G_{\min}^{\text{exc}} = 0.005 \mu\text{S}$, $G_{\max}^{\text{exc}} = 0.010 \mu\text{S}$, $G_{\min}^{\text{inh}} = 0.015 \mu\text{S}$, $G_{\max}^{\text{inh}} = 0.070 \mu\text{S}$.

Being a passive model, membrane potential did not provide firing, so we combined membrane potential-based firing rate with thresholding activation with accommodation. First, we computed an activation function from experimental data, which gave us firing rate as a function of membrane potential:

$$\text{Activation function} = FR_{\text{mem}}(V_{\text{mem}}) = \frac{20}{1 + \exp(-0.3 \cdot (V_{\text{mem}} + 60))}$$

A normalized version ($FR_{\text{mem}}^{\text{norm}}(V_{\text{mem}})$) which ranged from 0 to 1 was also computed. In parallel, we added firing dynamics with accommodation by first finding spiking times, or phases (θ_{spike}), whenever a rising V_{mem} crossed a threshold ($V_{\text{thr}} = -65 \text{ mV}$). We shifted a double exponential function defined as:

$$FR_{\text{accomm}}(\theta, \theta_{\text{spike}}) = \exp\left(\frac{-\theta - \theta_{\text{spike}}}{\varphi_{\text{decay}}}\right) - \exp\left(\frac{-\theta - \theta_{\text{spike}}}{\varphi_{\text{raise}}}\right)$$

where θ are theta phases, $\varphi_{\text{raise}} = 15 \text{ deg}$, and $\varphi_{\text{decay}} = 45 \text{ deg}$, to center its maximum over spikes. We normalized it by dividing by its maximum, and leaving a constant 10% activation, and 90% of dynamics:

$$FR_{\text{accomm}}^{\text{norm}}(\theta, \theta_{\text{spike}}) = 0.1 + 0.9 \cdot \frac{FR_{\text{accomm}}(\theta, \theta_{\text{spike}})}{\max(FR_{\text{accomm}}(\theta, \theta_{\text{spike}}))}$$

We then applied accommodation to firing rate distribution by combining both approaches:

$$FR = FR_{\text{mem}}^{\text{norm}}(V_{\text{mem}}(\theta)) \cdot FR_{\text{accomm}}^{\text{norm}}(\theta, \theta_{\text{spike}})$$

Biophysically realistic model

To expand and further validate our simulations with the simple conceptual model, we also used a more biophysically realistic pyramidal cell model (Navas-Olive et al., 2020) that integrates theta-modulated glutamatergic and GABAergic inputs, distributed along its somadendritic axis according as described in published experiments. To this purpose, we modified our former model at Github (<https://github.com/PridaLab/LCN-HippoModel/tree/place-field>). To simulate place fields, we modified the code used in the simple model by adding a place field asymmetric modulation to CA3, axo-axonic, PV-bc and CCK-bc synaptic conductances. Assuming a constant running speed of 30 cm/sec, and a linear track length of 60 cm, the place field started at 12 cm, the center was at 37.92 cm (at 72% of place field width, Harvey et al., 2009), and ended at 48 cm. As in the simple uni-compartmental model, theta modulation was multiplied by 1 outside the place field, and by the skewed place field modulation function (Figure S4A), whose ΔG_{inh} ranged from -1 to 1 , and ΔG_{exc} from 0 to 3 . However, simulations with $\Delta G_{\text{inh}} > 0.3$ were not considered because firing rate was too low to match the criteria to compute phase precession. These simulations were done using the synthetic cell with morphology n409 from the NeuroMorpho Turner archive, intrinsic individual 12 and synaptic individual 1, a generic synthetic cell that was not tuned to incorporate superficial (more CCK projections) or deep (more PV) microcircuits.

Extracellular recordings and behavior

Mice were initially anesthetized with 2% isoflurane and maintained under anesthesia with 0.75–1% isoflurane. 400 nL of pAAV-hDlx-GqDREADD-dTomato-Fishell-5 (Addgene plasmid #83897) was infused into the hippocampus (antero-posterior 2.0 mm, mediolateral 1.5 mm, dorsoventral 1.2 mm) at a rate of 25 nL/minute using a sharp glass pipette (15–20 nm in diameter), which was left in place for 15 minutes to minimize the backflow of virus. Following virus infusion, and in the same surgical procedure animals were implanted with 32-site, 4 shank μLED probes (NeuroLight, Plexon) over the dorsal right hippocampus (antero-posterior 2.0 mm, mediolateral 1.5 mm, dorsoventral 0.6 mm), as described previously (Valero et al., 2021, 2022; Zutshi et al., 2022). Ground and reference wires were implanted in the skull above the cerebellum, and a grounded copper mesh hat was constructed to shield the probes. Animals were allowed to recover for at least two weeks. Probes were mounted on microdrives that were advanced to CA1 pyramidal layer in small increments over 5 to 8 days, while depth distribution of LFPs (SPW-R events and theta oscillations) and unit firing were used to identify CA1 pyramidal layer.

After implantation, animals were handled daily and accommodated to the experimenter, recording room and cables for 1 week before the start of the experiments. Mice were trained to run laps in a PVC linear track (110 cm long, 6.35 cm wide) to retrieve water reward (5–10 μL) at each end. Water access was restricted and was only available as reward on a linear track, ad libitum for 30 minutes at the end of each experimental day and ad libitum for one full non-experimental day per week. The animal's position was monitored with a Basler camera (acA1300-60 gmNIR, Graftek Imaging) sampling at 30 Hz to detect a head-mounted red LEDs. Position was synchronized with neural data with TTLs signaling shutter position. Water delivery and optogenetic stimuli during track were controlled by a custom-made, Arduino-based circuit (circuits and software are available in <https://github.com/valegarman/HippoPlayground>). Electrophysiological data were acquired using an Intan RHD2000 system (Intan Technologies LLC) digitized with 30 kHz rate. The wide-band signal was downsampled to 1.25 kHz and used as the LFP signal. For a typical recording session,

mice were recorded continuously for ~500 min through 3 experimental blocks before and after chemogenetic manipulation: pre-track baseline (~100 min), Linear Maze task (~30 min), post-track baseline (~100 min), followed by an intraperitoneal injection of Clozapine N-oxide (CNO 5 mg/kg CNO in 1% DMSO) or Dimethylsulfoxide (1% DMSO in saline) injection and one more set of pre track-baseline, maze and post-track baseline recordings. CNO and DMSO sessions were interleaved, and we did not include in our analysis any recording sessions beyond the fourth day of CNO injection.

μ LEDs stimulation were conducted as described in (Valero et al., 2022). Briefly, μ LEDs were controlled with current (2–4.5 μ A generating 0.02–0.1 μ W of total light power; Valero et al., 2022) provided by a 12-channel current generator (OSC1Lite, NeuroNex Michigan Hub) driven by an Arduino (<https://github.com/valegarman/HippoPlayground>), which delivered trapezoid (1 ms rise time) blue light (centered emission at 460 nm, emission surface area = 150 mm²) 20 ms pulses at random sites with a randomly variable (40–60 ms) offset. Stimulation protocol was delivered for ~40 min during the pre-track baseline and post-track baseline epochs.

Unit clustering and neuron classification

Spike sorting was performed semi-automatically as previously described (Valero et al., 2021, 2022). Briefly, we employed our own pipeline KilosortWrapper (<https://github.com/brendonw1/KilosortWrapper>), a wrapper for KiloSort (<https://github.com/cortex-lab/KiloSort>). This was followed by manual adjustment of the waveform clusters using the software Phy (<https://github.com/kwikteam/phy>) and plugins for Phy designed in our laboratory (<https://github.com/petersenpeter/phy-plugins>). Following parameters were used for the Kilosort clustering: ops.Nfilt: 6 * numberChannels; ops.nt0: 64; ops.whitening: 'full'; ops.nSkipCov: 1; ops.whiteningRange: 64; ops.criterionNoiseChannels: 0.00001; ops.Nrank: 3; ops.nfullpasses: 6; ops.maxFR: 20000; ops.fshigh: 300; ops.ntbuff: 64; ops.scaleproc: 200; ops.Th: [4 10 10]; ops.lam: [5 20 20]; ops.nannealpasses: 4; ops.momentum: 1./[20 800]; ops.shuffle_clusters: 1. Unit clustering generated two clearly separable group (Petersen et al., 2021; Valero et al., 2021, 2022) based on their spike autocorrelograms, waveform characteristics and firing rate. Putative pyramidal cells and interneurons were tentatively separated based in these two clusters. A more reliable cell identity was assigned after inspection of all features, assisted by monosynaptic excitatory and inhibitory interactions between simultaneously recorded, well-isolated units and light responses by using the suite CellExplorer (Petersen et al., 2021; <https://cellexplorer.org>). Units were defined as optogenetically responsive cells (Valero et al., 2022) based on combination of three criteria: (i) an average firing response higher than 2 SD, (ii) significant modulation using a p value cutoff of 10^{−3}, and (iii) against randomly shuffled pulse times (500 replicates) and testing for significant difference between the observed value and the random distribution.

Place field and extracellular Spike-LFP coupling analysis

Firing rate distribution within place fields ('rate map') was generated as in (Valero et al., 2022). In summary, spiking data was binarized into 2.2 cm wide bins, and spike counts were normalized by time occupancy (smoothing size: 2 bins) for epochs when the animal's speed was >1 cm/s. Trials for forward and backward directions were evaluated separately. Place fields were defined from these rate maps as previously described (Fernández-Ruiz et al., 2017; Mizuseki et al., 2011; Valero et al., 2022). The field boundaries were defined when the rate decreased below 20% of the peak firing rate. Place fields cleared all criteria when they were between 8.75 cm and 75 cm wide, had a minimum peak firing rate of 3 Hz and a spatial coherence >0.7. Place field stability was defined by correlating rate/bin distributions (Spearman correlation) for the first and second maze exploration. Standard deviation was computed across all spatial bins for both run directions (100 bins in total). Spatial coherence per cell was estimated as the mean correlation between the firing rate in each spatial bin and the corresponding rates averaged over the ± 4 nearest-neighbor bins (Muller and Kubie, 1989). We also calculated the spatial information content in bits per spike (Souza et al., 2018) as following:

$$SPI = \sum_K P_{K|x_i} \log_2 \frac{P_{K|x_i}}{P_K}$$

where P_K is the probability of observing a rate K and $P_{K|x_i}$ is the conditional probability of observing a rate K in position x_i .

The mutual information between the position and firing rate (MI_{rate}) (Souza et al., 2018) was estimated as following:

$$MI_{Rate} = \sum_i \sum_j p_{ij} \log_2 \left(\frac{p_{ij}}{p_i \cdot p_j} \right)$$

where p_i and p_j are the probabilities of the i_{th} position bin and the j_{th} firing rate bin, respectively, and p_{ij} is the joint probability between position i_{th} and firing rate j_{th} .

The theta-band phase of the LFP recorded at the highest theta power channel above CA1 *stratum pyramidale* was estimated as the Hilbert transform of the narrowband filtered LFP (5–11 Hz). Theta epochs were detected automatically using the ratio of the power in theta band (5–11 Hz) to the power of nearby bands (1–4 Hz, 12–14 Hz) of CA1 LFP (Fernández-Ruiz et al., 2017). Theta modulation indices for each neuron were estimated as described for intracellularly recorded cells. For phase precession analysis, the instantaneous theta phases (from the filtered CA1 pyramidal layer LFP) of spikes were plotted against the linearized positions in the track for each place field (Fernández-Ruiz et al., 2017). Circular-linear regression between position and theta phase was applied to calculate the phase-precession slope and correlation strength, where a correlation coefficient, similar to the Pearson's correlation, was obtained. For further analyses, only fields displaying significant phase-position correlation ($p < 0.05$) were considered. Mutual information between the position and firing phase was estimated as following:

$$MI(\text{Phase}, \text{Position}) = H(\text{Phase}) + H(\text{Position}) - H(\text{Phase}, \text{Position})$$

where entropies $H(\text{position})$ and $H(\text{phase})$ are defined as:

$$H(x) = - \sum_i p(x_i) \log p(x_i)$$

and joint entropy $H(x, y)$ is:

$$H(x, y) = - \sum_i \sum_j p(x_i, y_j) \log p(x_i, y_j)$$

Mutual information function from MATLAB's Information Theory Toolbox was used (Chen, 2022).

Subsampling for rate maps were performed to replicate pyramidal spiking suppression after CNO with respect to DMSO injection (68.35%). All of the subsampled analyses were performed from scratch following the same code as with the original data but adding a step in which 30% of spikes were randomly discarded in a uniform way along all the session. The analysis was performed using the remaining 70% of spikes. The only analysis that was not performed from scratch was the slope computation: slopes were computed using the subset of the subsampled spikes that fell within place fields computed with the original data. Slopes that were not significant were discarded.

Assembly analysis

Cell assemblies were defined using an unsupervised statistical framework based on a hybrid PCA followed by ICA (Lopes-dos-Santos et al., 2013) as previously described (Valero et al., 2022; Zutshi et al., 2022). Spike trains of each neuron were binned in 25-ms intervals and z-scored firing rates were calculated for each bin. Spike trains were convolved with a Gaussian kernel (standard deviation = 10 ms), and the matrix of firing correlation coefficients for all pairs of neurons was constructed. Next, using the fast-ICA algorithm, we determined the vector of weights (contribution of each neuron) for each assembly(component). Most of the detected assembly patterns consisted of a few neurons with high weights and a large group of neurons with weights around zero (Figure 6I). The fraction of assemblies increasing or decreasing in expression was defined by calculating a threshold of mean ± 1 standard deviation during baseline sessions and measuring the fraction of assemblies whose expression changed greater than, or less than this threshold after DMSO/CNO injection or downsampling.

Histological processing and microscopy

Mice or rats were overdosed with pentobarbital injection (100 mg/kg body weight), perfused with saline and 4% paraformaldehyde before their brains were rapidly removed. After overnight post-fixation in 4% paraformaldehyde solution, the brain was washed 3 times in 0.1 M phosphate buffered saline. Coronal sections of 50–100 μm thickness were cut using a Leica Microsystems VT 1000S vibratome, wash 3–4 times in 0.1 M phosphate buffer (PB) and stored in 0.1 M PB with 0.05% sodium azide at 4°C. Sections were mounted on glass slides in VectaShield (Vector Laboratories) and observed with epifluorescence (Leitz DMRB microscope, Leica) or confocal imaging (Zeiss). For the identification of native EYFP + or streptavidin + neurons and layer markers we proceeded as previously described (35, 45). Sections containing Neurobiotin-labeled cells were localized by incubating them in 1:400 Alexa Fluor488-conjugated streptavidin (Jackson ImmunoResearch 016-540-084) with 0.5% Triton X-100 (vol/vol) in PBS (PBS-Tx) for 2 h at 22–25°C.

QUANTIFICATION AND STATISTICAL ANALYSIS

Statistical analysis

All statistical analyses were performed with standard and custom-made MATLAB functions (<https://github.com/valegarman/HippoCookBook>). No specific analysis was used to estimate minimal population sample, but the number of animals, trials, and recorded cells were larger or similar to those employed in previous works (Valero et al., 2017, 2021, 2022). All data presented here were obtained from experimental replicates with at least three independent experimental repeats for each assay. All attempts of replication were successful. Data collection was not performed blinded to the subject conditions. Data analysis was performed blinded to the scorer or did not require manual scoring. All subjects underwent the same number of conditions (unless stated otherwise) in a randomly assigned fashion. Unless otherwise noted, for all tests, non-parametric two-tailed Wilcoxon's paired signed-rank test and Kruskal-Wallis one-way analysis of variance. When parametric two-ways ANOVA test were used, the data satisfied the criteria for normality (Kolmogorov–Smirnov test) and equality of variance (Bartlett's test for equal variance). For multiple comparisons, Tukey's honesty post hoc test was employed and the corrected $p < 0.05$, $**p < 0.01$, $***p < 0.001$ are indicated. p-values for Spearman's correlations are computed using a Student's t distribution for a transformation of the correlation. Results are displayed as boxplots representing median, 25th/75th percentiles and data range. Dispersion represents $\pm \text{CI}_{95}$ around mean. The exact number of replications for each experiment is detailed in the text and figures.

Cell Reports, Volume 40

Supplemental information

**Inhibitory conductance controls place
field dynamics in the hippocampus**

Manuel Valero, Andrea Navas-Olive, Liset M. de la Prida, and György Buzsáki

SUPPLEMENTAL ITEMS

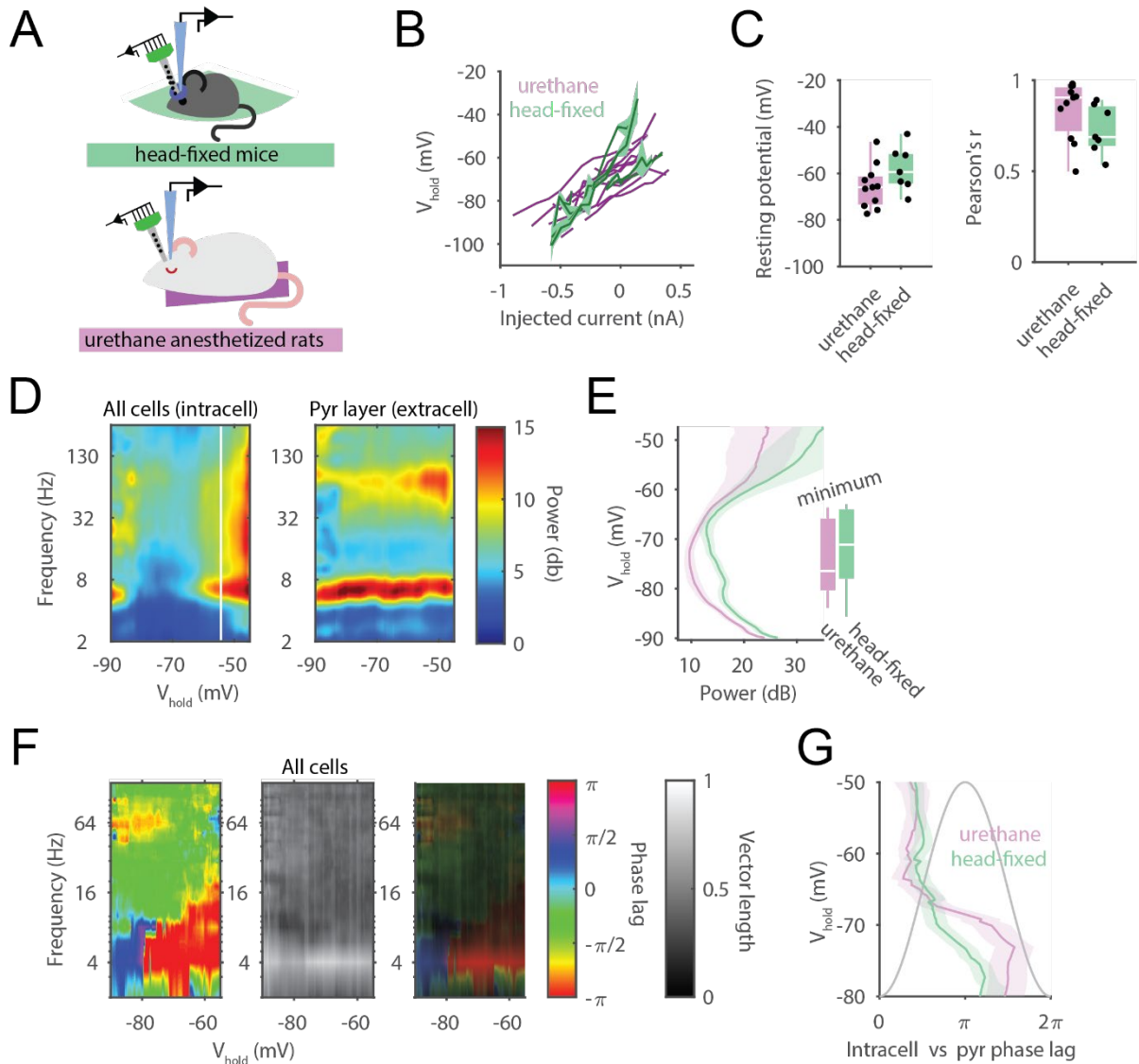


Figure S1: Intracellular recordings in anesthetized rats and head-fixed mice. Related to figure 2. **(A)** Schematic of the in vivo intracellular experiments. CA1 pyramidal neurons were recorded with sharp pipettes simultaneously with local field potentials using 16 to 64-channel silicon probes in head-fixed mice and urethane anesthetized rats. **(B)** Current-Voltage (I-V) curve (mean \pm CI95) for 11 cells from 10 anesthetized rats (purple) and 7 cells from 4 head-fixed mice (green). **(C)** Average resting potentials ($\chi^2_{1,17} = 3.12$, $P = 0.077$, Kruskal-Wallis (KW) Test) and Pearson's correlation coefficient of the I-V curve ($\chi^2_{1,17} = 2.26$, $P = 0.152$, KW Test) for all cells recorded in anesthetized and head-fixed animals. **(D)** Averages of intracellular power density spectra at different holding potentials for all recorded cells (left). Theta power of V_m has a minimum at around -75 mV. Spectra of extracellular LFPs obtained from the same theta epochs for reference. **(E)** Theta power of V_m for cells recorded in anesthetized and head-fixed animals. No differences were found in the curve minima across groups ($\chi^2_{1,17} = 0.39$, $P = 0.532$, KW Test) nor the power- V_{hold} curves (preparation general effects: $F_{1,2136} = 1.01$, $P = 0.5$; V_{hold} general effects: $F_{1,2136} = 5.11$; $P = 0.023$, two-ways ANOVA). **(F)** Intracellular-extracellular phase lag spectra at different holding potentials (left) and vector length spectra of the intracellular-extracellular phase lags (middle) for all recorded cells and combined heatmap (right). Note large phase jump below -75 mV. **(G)** Cells recorded from anesthetized rats and head-fixed mice showed a similar theta phase reversal of V_m (species general effects: $F_{1,818} = 12.67$, $P = 0.17$; V_{hold} general effects: $F_{1,818} = 10.49$; $P = 0.0013$, two-ways ANOVA).

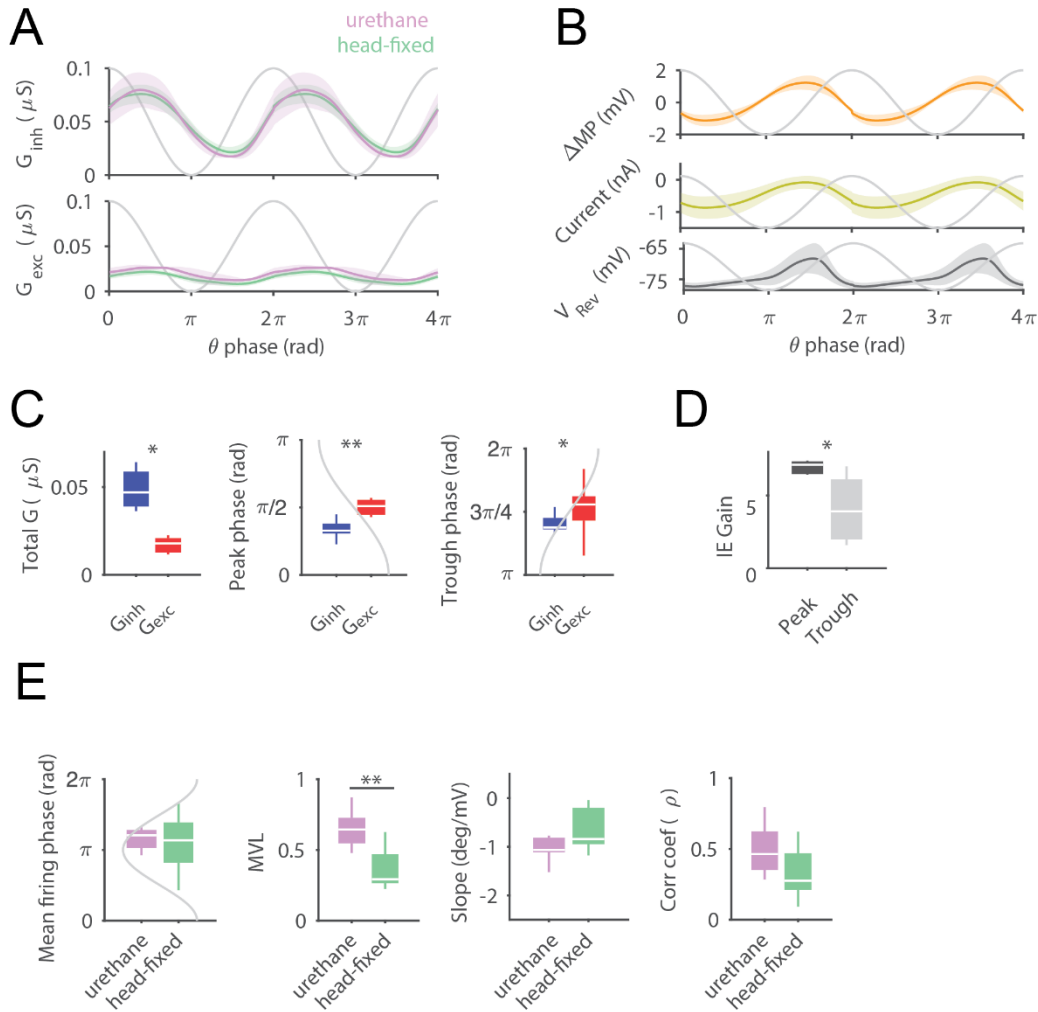


Figure S2: Excitatory and inhibitory conductances during theta oscillations. Related to figures 2 and 3. **(A)** Average excitatory (G_{exc}) and inhibitory (G_{inh}) conductances estimated for 11 cells from 10 anesthetized rats (purple) and 7 cells from 4 head-fixed mice (green). Similar G_{inh} and G_{exc} dynamics were found across both preparations (preparation general effects: $F_{1,696} = 0.64$, $P = 0.42$; phase general effects: $F_{1,696} = 291.82$; $P = 0.037$). **(B)** Average V_m change (ΔMP , top), estimated synaptic currents (middle) and voltage reversal (V_{rev}) (bottom) for all cells. **(C)** Average values across all theta bins (left; $Z = 28$, $P = 0.016$, Wilcoxon signed rank (WSR) test), peak phase (middle; $Z_{MS} = 10.5$, $P = 0.001$; Multiple-sample (MS) test for equal median directions) and trough phase (right; $Z_{MS} = 4.67$, $P = 0.031$; MS test) for G_{inh} and G_{exc} for all cells. **(D)** Inhibitory-to-excitatory ratios for the estimated conductances ($Z = 28$, $P = 0.016$; WSR test). **(E)** Differences between the intracellular and head-fixed experiments for preferred firing phase (left; $Z_{MS} = 0.18$; $P = 0.66$; MS test), mean vector length (MVL, middle-left; $\chi^2_{1,17} = 9.64$, $P = 0.002$, KW Test), voltage-phase slope (middle-right; $\chi^2_{1,17} = 1.48$, $P = 0.22$, KW Test) and Spearman's correlation coefficient of the voltage-phase slope relationship (right; $\chi^2_{1,17} = 2.38$, $P = 0.12$, KW Test). * $P < 0.05$, ** $P < 0.001$.

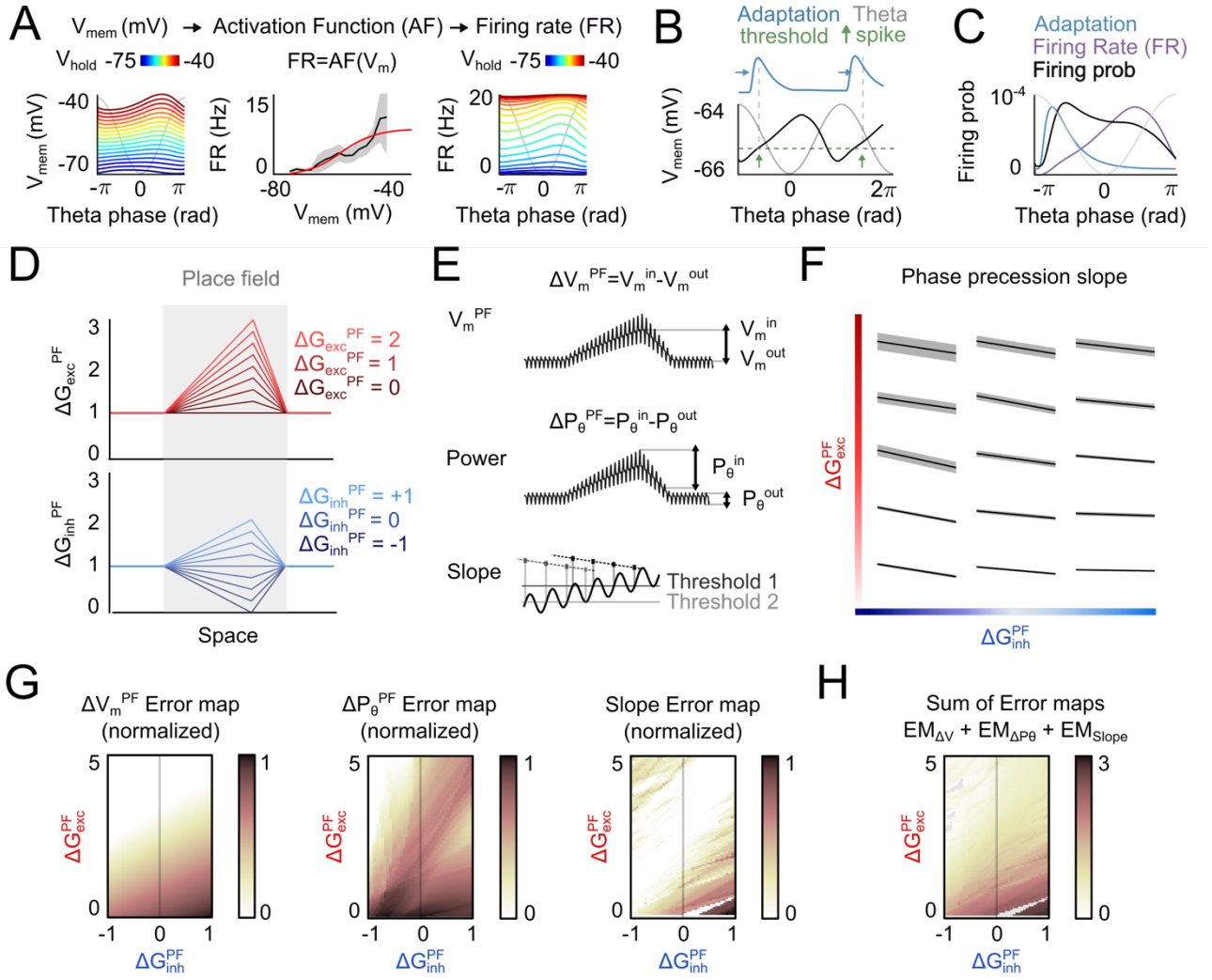


Figure S3: Firing probability distribution and spatial modulation in the conductance-based model.

Related to figures 3 and 4. **(A)** Scheme to obtain firing rate distribution from membrane potential: an experimental activation function (AF) is used to transform V_{m} to firing rate. Each color represents V_{m} (left) and firing rate distribution (right) at different holding potentials. **(B)** In order to induce spikes from membrane potentials and take into consideration of spike adaptation, each time a rising membrane potential (V_{m}) crossed certain threshold (green) a “spike” event was assigned (green arrow). Adaptation (blue) was defined as a double exponential function centered at spike time. **(C)** Final firing probability distribution (black) was obtained as the convolution of firing rate distribution (purple) and an adaptation function that resulted from the thresholded spikes (blue). **(D)** Spatial modulation of excitation (top, $\Delta G_{\text{exc}}^{\text{PF}}$) and inhibition (down, $\Delta G_{\text{inh}}^{\text{PF}}$). Inside the place field, V_{m} modulation follows a skewed distribution whose maximum is the value indicated by ΔG^{PF} ($\Delta G_{\text{exc}}^{\text{PF}}$ ranges from 0 to 5, $\Delta G_{\text{inh}}^{\text{PF}}$ from -1 to 1). There is no modulation outside the place field, so $\Delta G^{\text{PF}} = 1$. **(E)** Scheme of the computation of three measures used to compare results from our model to experimentally observed values. (Top) Difference of the membrane potential ($\Delta V_{\text{m}}^{\text{PF}}$) is computed as the difference between the mean V_{m} inside versus outside of place field. (Middle). Difference in power ($\Delta P_{\theta}^{\text{PF}}$) is computed as the difference between the mean intracellular theta amplitude inside versus outside of place field. (Bottom) Phase precession slopes were calculated for spikes obtained using a set of thresholds ranging from -65.3mV to -49.3mV . **(F)** Same $\Delta G_{\text{exc}}^{\text{PF}}$ vs $\Delta G_{\text{inh}}^{\text{PF}}$ map as Fig. 4A showing phase precession slopes; mean \pm SD was plotted. **(G)** Error maps for $\Delta V_{\text{m}}^{\text{PF}}$ (left), $\Delta P_{\theta}^{\text{PF}}$ (middle) and slope (left), computed as the simulated values (maps of Fig.4B) minus the closest experimental values from the given range (Table 1). Maps are normalized to 1. **(H)** Sum of the three error maps (EM) of **G** to illustrate map locations with minimum error.

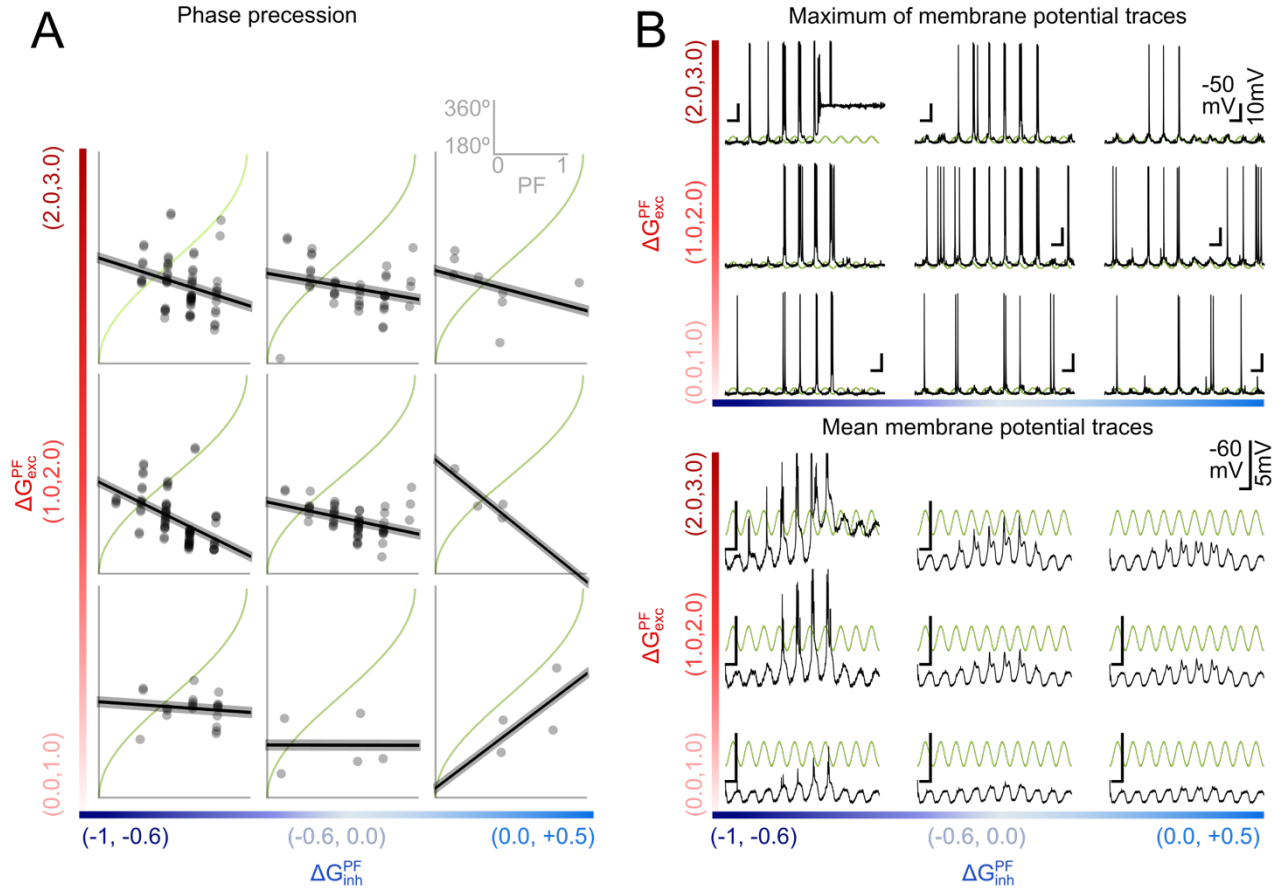


Figure S4: Multi-compartment Hodgkin-Huxley CA1 neuron model. Related to figure 4. **(A)** Simulations in the multi-compartment CA1 neuron model (Navas-Olive et al., 2020) were merged in groups depending on their ΔG_{exc}^{PF} and ΔG_{inh}^{PF} values (ΔG_{exc}^{PF} , was grouped on three intervals: 0.0 to 1.0, 1.0 to 2.0 and 2.0 to 3.0; ΔG_{inh}^{PF} on: -1.0 to -0.6, -0.6 to 0.0, and 0.0 to +0.5). Maximum V_m value of any simulation for each timestamp was plotted to illustrate all spikes (top) and V_m dynamics (bottom). Reference theta oscillation is displayed in green. **(B)** Phase vs place field location plots (spikes of several simulations were merged). Each horizontal sub-axis shows place field from beginning (left) to end (right), and vertical sub-axes show theta phase from 180° (theta peak) to 360° (theta trough) (plotted in green to ease visualization).

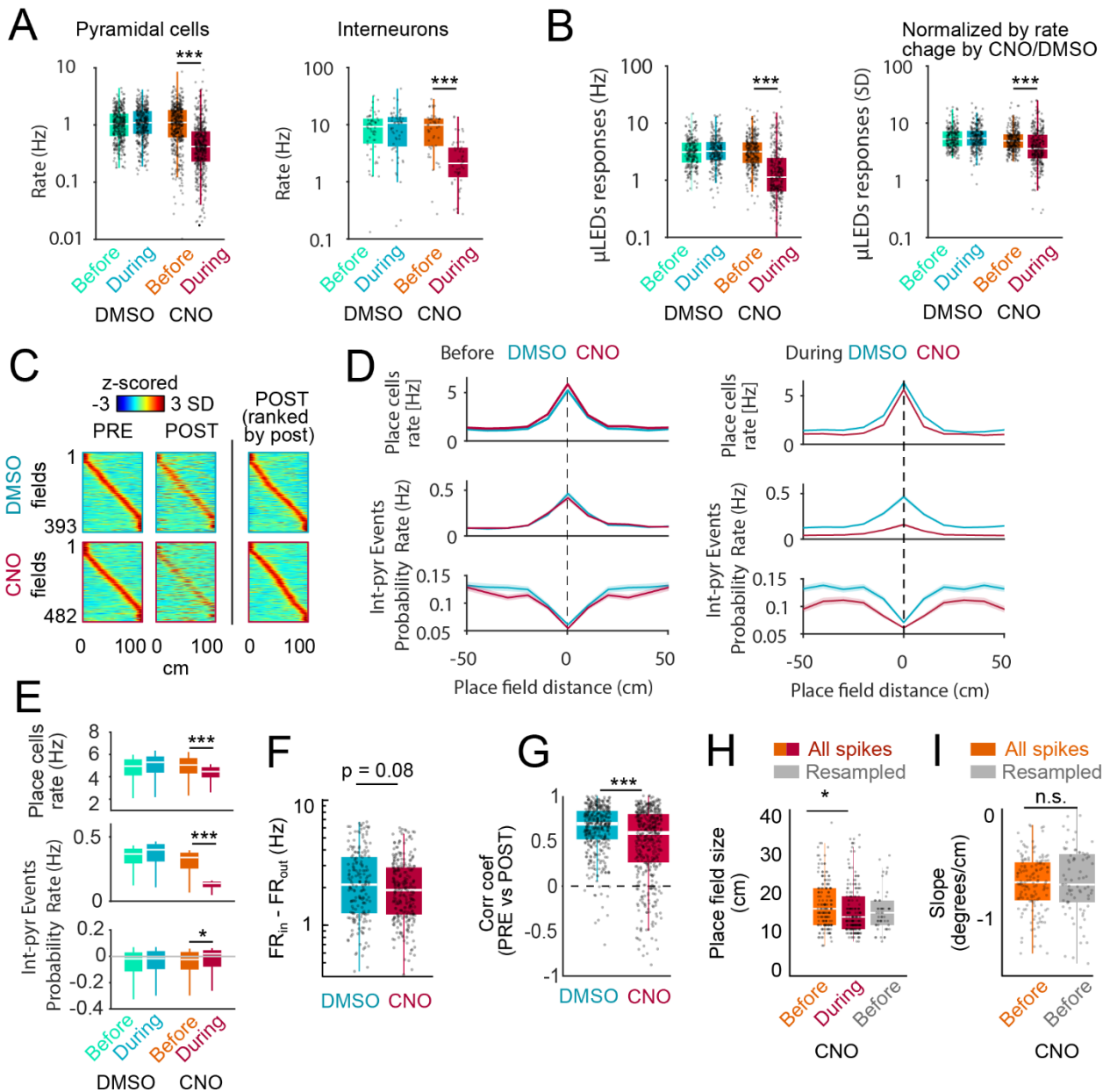


Figure S5: Characterization of the chemogenetic manipulations spiking features of CA1 neurons.

Related to figure 5 and 6. **(A)** Group differences in the firing rate of all pyramidal cells before and after CNO/DMSO injections (left). Activating GABAergic cells by dlx5/6-Gq-DREADD after CNO injection decreased firing rates of pyramidal cells (DMSO/CNO general effects: $F_{1,1710} = 142.15$, $P < 10^{-31}$; Before/After effects: $F_{1,1710} = 83.01$; $P < 10^{-19}$; interaction: $F_{1,1710} = 111.55$, $P < 10^{-25}$, two-ways ANOVA). Interneurons show a paradoxical firing rate decrease after CNO (right; DMSO/CNO general effects: $F_{1,202} = 18.76$, $P < 10^{-4}$; Before/After effects: $F_{1,202} = 19.64$; $P < 10^{-4}$; interaction: $F_{1,202} = 19.96$, $P < 10^{-4}$, two-ways ANOVA). **(B)** Firing rates in response to μ LEDs stimulation for light-responsive pyramidal cells before and during CNO (DMSO/CNO general effects: $F_{1,1096} = 92.88$; $P < 10^{-20}$; Before/After effects: $F_{1,1096} = 82.78$; $P < 10^{-18}$; interaction: $F_{1,1096} = 96.98$, $P < 10^{-21}$, two-ways ANOVA). Group differences persist after normalizing by baseline firing rate (Z-scored, right) (DMSO/CNO general effects: $F_{1,1096} = 49.57$; $P < 10^{-11}$; Before/After effects: $F_{1,1096} = 20.78$; $P < 10^{-5}$; interaction: $F_{1,1096} = 22.34$, $P < 10^{-5}$, two-ways ANOVA). **(C)** Z-scored place fields of pyramidal cells before (PRE, left) and during (POST; middle) CNO (bottom) or DMSO (top) injection sorted by place field position in PRE (left panels). Right panels, place fields during CNO (bottom) or DMSO (top) sorted by POST. **(D)** Peri-place field firing rate averages (mean \pm CI95) of all place fields (top), rate of interneuron-place cell spike pair events (interneuron spikes at less than 3 ms prior to the spike of the reference place cell, START Methods) (middle), and rate-normalized interneuron-place cell spike pair events (bottom) before (left) and after DMSO and CNO injections (right). Note that interneuron-place cell co-occurrence in the monosynaptic time window is decreased within the place field, implying weaker inhibition of place cells within their place fields. **(E)** Group differences in peri-place field rate (top; DMSO/CNO general effects: $F_{1,7633} = 208.81$; $P < 10^{-45}$; Before/After effects: $F_{1,7633} = 29.06$; $P < 10^{-7}$; interaction: $F_{1,7633} = 247.27$, $P < 10^{-54}$), and interneuron-place cell spike pair events rate (middle: DMSO/CNO general effects: $F_{1,7633} =$

1949.3; $P < 10^{-99}$; Before/After effects: $F_{1, 7633} = 573.72$; $P < 10^{-121}$; interaction: $F_{1, 7633} = 960.40$, $P < 10^{-197}$) and probability (bottom: DMSO/CNO general effects: $F_{1, 7633} = 1.71$; $P = 1.74$; Before/After effects: $F_{1, 7633} = 8.57$; $P = 0.0034$; interaction: $F_{1, 7633} = 2.26$, $P = 0.13$, two-ways ANOVA). (F) Group effects between in-field and out-field firing rates after CNO/DMSO ($\chi^2_{1,440} = 3.07$, $P = 0.079$, KW test). (G) Place cell rate stability (Spearman's ρ) after injection for DMSO and CNO groups ($\chi^2_{1,346} = 28.15$, $P < 10^{-6}$, KW Test). (H) The place field size decreased after CNO versus DMSO injection was explained by the overall all rate decrease ($\chi^2_{2,385} = 8.17$, $P = 0.017$, KW Test) and/or the in-field rate reduction (see Figure 6C). (I) No differences were observed in the phase precession slope after resampling spikes to match CNO effects ($\chi^2_{1,222} = 0.27$, $P = 0.60$, KW Test). * $P < 0.05$, ** $P < 0.01$, *** $P < 0.001$.

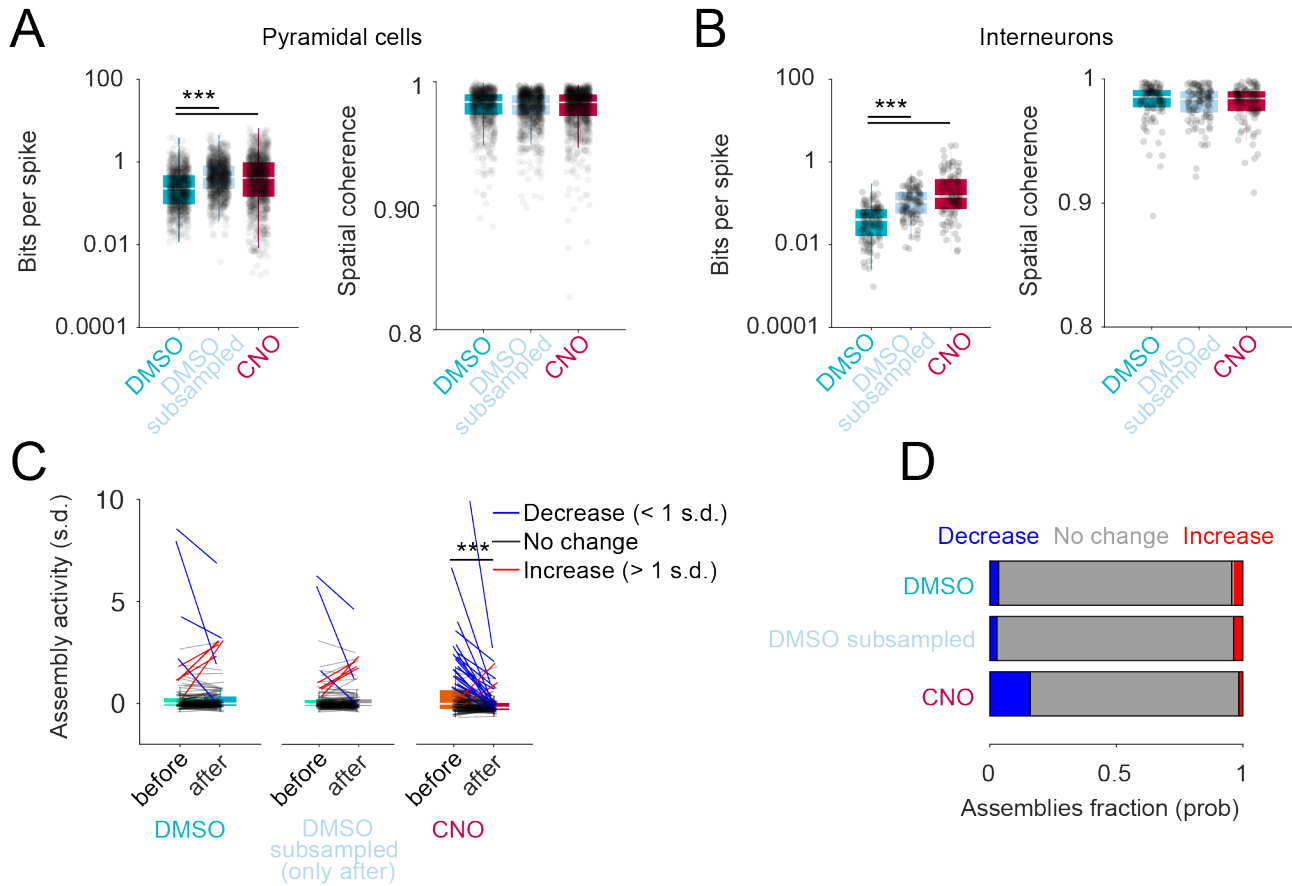


Figure 6: Effect of CNO-Dlx-Gq DREADDs on spatial metrics and assemblies' dynamic expression.

Related to figure 5 and 6. (A) Information content in bits per spike ($\chi^2_{2,2236} = 149.64$, $P < 10^{-32}$, KW Test) and spatial coherence ($\chi^2_{2,2236} = 2.91$, $P = 0.23$, KW Test) for all pyramidal cells' firing fields before and after CNO/DMSO injections (left). The apparent increase in bits per spike could be explained by the firing rate change induced by CNO (B) Same as in A for interneurons (bits per spike: $\chi^2_{2,323} = 88.37$, $P < 10^{-19}$; spatial coherence: $\chi^2_{2,323} = 1.09$, $P = 0.59$, KW Test). (C) Activity for all detected assemblies before and after DMSO ($n = 114$, signed rank = 3203, $P = 0.83$, Wilcoxon paired signed-rank test) or CNO injection ($n = 125$, signed rank = 6117, $P < 10^{-7}$, Wilcoxon paired signed-rank test). No differences were found when the DMSO condition was downsampled after injection to match the firing rates of the CNO condition (signed rank = 2810, $P = 0.80$, Wilcoxon paired signed-rank test). (D) CNO, but no DMSO, decreased the incidence of cell assemblies identified before injection ($\chi^2 = 2.55$, $P = 0.0013$, χ^2 Goodness of Fit Test). This result could not be explained by the CNO-induced decrease of firing rate alone ($\chi^2 = 0.028$, $P = 0.99$, χ^2 Goodness of Fit Test). *** $P < 0.001$.

Table S1: Three signatures of place fields in CA1 pyramidal cells. Related to figure 4.

Place field signature	Place field amplitude (mV) [*]	Theta power (in/out ratio) [§]	Phase precession (cycl/field)
(Harvey et al., 2009)	5.7 ± 2.9	2.12 ± 0.4	Not reported
(Lee et al., 2012)	Not reported	1.40 ± 0.10	Not reported
(Bittner et al., 2015)	6.9 ± 1.0	Not reported	Not reported
(Grienberger et al., 2017)	6.2 ± 0.7	1.41 ± 0.02	Not reported
(Cohen et al., 2017)	4.8 ± 0.8	Not reported	Not reported
(Epsztein et al., 2011)	11.5 ± 1.6	Not reported	Not reported
(Zhao et al., 2020)	7.7 ± 1.5	2.0 ± 0.2	Not reported
(Zutshi et al., 2022)	Not reported	Not reported	-0.61 ± 0.20
(Oliva et al., 2016)	Not reported	Not reported	-0.82 ± 0.17
This manuscript (Fig. 6G)	Not reported	Not reported	-0.69 ± 0.15
Mean ± SD	7.02 ± 2.62	1.73 ± 0.38	-0.71 ± 0.11
Median ± IQR	6.2 ± 2.57	1.70 ± 0.65	-0.69 ± 0.15

^{*}Place field amplitude from Zhao et al., (2020) derived after subtracting baseline from ramp depolarization amplitude. [§]Theta power change from Grienberger et al., (2017) derived from in/out-field theta envelope percentage changes. Theta power change in Zhao et al., (2020) was derived from baseline and in-field ratio of theta amplitude.